Astroparticle Physics 163 (2024) 103007

Contents lists available at ScienceDirect

Astroparticle Physics

journal homepage: www.elsevier.com/locate/astropartphys

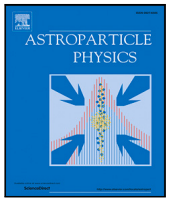

Detection limits and trigger rates for ultra-high energy cosmic ray detection with the EUSO-TA ground-based fluorescence telescope

J.H. Adams Jr. [1], L. Anchordoqui [2], D. Barghini [3,4,5], M. Battisti [6,5,4], A.A. Belov [7], J.W. Belz [8], M. Bertaina [4,5], F. Bisconti [9,5,*], C. Blaksley [10], S. Blin-Bondil [6,11], F. Capel [12], M. Casolino [9,13,10], A. Cummings [14], T. Ebisuzaki [10], J. Eser [15], S. Falk [16], F. Fenu [17], S. Ferrarese [4,5], G. Filippatos [15], M. Fouka [18], C. Fuglesang [19], P. Gorodetzky [6], F. Guarino [20,21], A. Haungs [16], N. Inoue [22], F. Kajino [23], P.A. Klimov [7], M. Manfrin [4,5], L. Marcelli [9], W. Marszał [24], H. Mashiyama [22], J.N. Matthews [8], H. Miyamoto [4,5], S. Ogio [25], H. Ohmori [10], A.V. Olinto [15], E. Parizot [6,26], T. Paul [2], P. Picozza [9,13], L.W. Piotrowski [27], Z. Plebaniak [13,9], G. Prévôt [6], M. Przybylak [28], E. Reali [13,9], M. Ricci [29], H. Sagawa [25], Z. Sahnoun [18], N. Sakaki [10], H. Shin [30,31], K. Shinozaki [24], P. Sokolsky [8], J. Szabelski [32], N. Tajima [10], Y. Takizawa [10], Y. Tameda [33], G.B. Thomson [8], M. Vrabel [24], L. Wiencke [34], M.Yu. Zotov [7]

[1] *University of Alabama in Huntsville, Huntsville, AL, USA*
[2] *Lehman College, City University of New York (CUNY), New York, NY, USA*
[3] *Osservatorio Astrofisico di Torino, Istituto Nazionale di Astrofisica, Turin, Italy*
[4] *Dipartimento di Fisica, Università di Torino, Turin, Italy*
[5] *Istituto Nazionale di Fisica Nucleare - Sezione di Torino, Turin, Italy*
[6] *Université de Paris, CNRS, AstroParticule et Cosmologie, Paris, F-75013, France*
[7] *Skobeltsyn Institute of Nuclear Physics, Lomonosov Moscow State University, Moscow, Russia*
[8] *University of Utah, Salt Lake City, UT, USA*
[9] *Istituto Nazionale di Fisica Nucleare - Sezione di Roma Tor Vergata, Rome, Italy*
[10] *RIKEN, Wako, Japan*
[11] *Omega, Ecole Polytechnique, CNRS/IN2P3, Palaiseau, France*
[12] *Max Planck Institute for Physics, Munich, Germany*
[13] *Università di Roma Tor Vergata - Dipartimento di Fisica, Rome, Italy*
[14] *Pennsylvania State University, State Collage, PA, USA*
[15] *University of Chicago, Chicago, IL, USA*
[16] *Karlsruhe Institute of Technology (KIT), Eggenstein-Leopoldshafen, Germany*
[17] *Agenzia Spaziale Italiana, Via del Politecnico, Rome, 00133, Italy*
[18] *Dep. Astronomy, Centre Res. Astronomy, Astrophysics and Geophysics (CRAAG), Algiers, Algeria*
[19] *KTH Royal Institute of Technology, Stockholm, Sweden*
[20] *Istituto Nazionale di Fisica Nucleare - Sezione di Napoli, Naples, Italy*
[21] *Università di Napoli Federico II - Dipartimento di Fisica "Ettore Pancini", Naples, Italy*
[22] *Saitama University, Saitama, Japan*
[23] *Konan University, Kobe, Japan*
[24] *National Centre for Nuclear Research, Otwock, Poland*
[25] *Institute for Cosmic Ray Research, University of Tokyo, Kashiwa, Japan*
[26] *Institut Universitaire de France (IUF), Paris, France*
[27] *Faculty of Physics, University of Warsaw, Warsaw, Poland*
[28] *University of Lodz, Faculty of Physics and Applied Informatics, Department of Astrophysics, Lodz, 90-236, Poland*
[29] *Istituto Nazionale di Fisica Nucleare - Laboratori Nazionali di Frascati, Frascati, Italy*
[30] *Graduate School of Science, Osaka Metropolitan University, Sugimoto, Sumiyoshi, Osaka, 558-8585, Japan*
[31] *Nambu Yoichiro Institute of Theoretical and Experimental Physics, Osaka Metropolitan University, Sugimoto, Sumiyoshi, Osaka, 558-8585, Japan*
[32] *Stefan Batory Academy of Applied Sciences, Stefana Batorego 64C, Skierniewice, 96-100, Poland*
[33] *Osaka Electro-Communication University, Neyagawa, Japan*

* Corresponding author at: Istituto Nazionale di Fisica Nucleare - Sezione di Roma Tor Vergata, Rome, Italy.
E-mail address: francesca.bisconti@roma2.infn.it (F. Bisconti).

https://doi.org/10.1016/j.astropartphys.2024.103007
Received 23 January 2024; Received in revised form 31 May 2024; Accepted 24 June 2024
Available online 1 July 2024

[34] Colorado School of Mines, Golden, CO, USA

ARTICLE INFO

Keywords:
Cosmic rays
Fluorescence detector
Cherenkov detector
Simulations
Data analysis

ABSTRACT

EUSO-TA is a ground-based fluorescence telescope built to validate the design of ultra-high energy cosmic ray fluorescence detectors to be operated in space with the technology developed within the Joint Exploratory Missions for Extreme Universe Space Observatory (JEM-EUSO) program. It operates at the Telescope Array (TA) site in Utah, USA. With an external trigger provided by the Black Rock Mesa fluorescence detectors of the Telescope Array experiment, with EUSO-TA we observed air-showers from ultra-high energy cosmic rays, as well as laser events from the Central Laser Facility at the TA site and from portable lasers like the JEM-EUSO Global Light System prototype. Since the Black Rock Mesa fluorescence detectors have a ∼30 times larger field of view than EUSO-TA, they allow a primary energy reconstruction based on the observation of a large part of the shower evolution, including the shower maximum, while EUSO-TA observes only a part of it, usually far away from the maximum. To estimate the detection limits of EUSO-TA in energy and distance, a method was developed to re-scale their energy, taking into account that EUSO-TA observes only a portion of the air-showers. The method was applied on simulation sets with showers with different primaries, energy, direction, and impact point on the ground, as well as taking into account the experimental environment. EUSO-TA was simulated with an internal trigger and different elevation angles and electronics. The same method was then applied also to real measurements and compared to the simulations. In addition, the method can also be used to estimate the detection limits for experiments that are operated at high altitudes and in most cases can see the maximum of the showers. This was done for EUSO-SPB1, an instrument installed on a super-pressure balloon. Finally, the expected detection rates for EUSO-TA were also assessed using the prepared simulated event sets. The rates correspond to a few detections per recording session of 30 h of observation, depending on the background level and the configuration of the detector.

1. Introduction

One of the aims of the JEM-EUSO program [1] is to build a fluorescence cosmic ray detector designed to observe Ultra-High Energy Cosmic Rays (UHECRs) from space. The UHECRs of interest have energy $\gtrsim 5 \times 10^{19}$ eV. As deflections due to the extra-galactic and galactic magnetic fields decrease with the energy, at these energies the possibility of identifying the astrophysical sources is enhanced. Moreover, a strong suppression in the flux observed at such energies could be consistent with the Greisen–Zatsepin–Kuzmin (GZK) cutoff [2,3], photo-disintegration of primaries, or the maximum power of sources. The origin of the suppression is still debated and subject of studies. However, the observation of such cosmic rays is challenging because of their low flux of ∼1 particle/km^2/millennium. The advantage of observations from space is that the detection aperture is higher from space with respect to ground, since the observed area projected on the ground would be up to $\sim 10^5$ km^2, much larger than any current ground-based experiments that cover areas of $\sim 10^3$ km^2. In this context, UHECRs can be detected by observing the UV fluorescence light emitted isotropically by nitrogen molecules when extensive air showers (hereafter called simply "showers") induced by UHECRs cross the atmosphere, which acts as a huge calorimeter. When UHECRs cross the atmosphere, there is also Cherenkov emission, occurring when charged particles cross a medium with a speed higher than the speed of light in that medium. This emission happens in a cone around the direction of the shower development and both direct and scattered Cherenkov photons can be detected by fluorescence detectors as well.

EUSO-TA [4,5] is one of the experiments of the JEM-EUSO program, developed and operated to validate the observation principle and the design of the JEM-EUSO detectors, by observing showers and laser pulses from the ground. It is installed at the Telescope Array (TA) [6] site in Utah (USA), in front of the Black Rock Mesa Fluorescence Detector (TA-BRM-FD) station [7], as shown in Fig. 1. With the external trigger provided by the TA-BRM-FDs, it is possible to detect showers and pulsed lasers from the Central Laser Facility (CLF) [8] located about 21 km away, which can be used to test and calibrate the detector. In addition, portable lasers with adjustable direction and energy, like the Global Light System prototype (GLS) [9], can be used to vary the distance and direction of the source from the detector.

This paper provides updates to the analysis discussed in [4]. It describes the estimation of the detection limit of EUSO-TA, i.e. the energy required to detect showers varying the distance, taking into account that EUSO-TA observes only a portion of their development. Taking into account that in the energy range considered in this analysis, both the light and heavy components are present [10], both proton and iron were simulated as primary cosmic rays. The idea is to obtain results for both the primaries, expecting that the actual limits are in between them. The detection limit for EUSO-TA was re-scaled to estimate the limit of EUSO-SPB1, that operated from a super-pressure balloon in 2017, considering the different detection efficiencies and atmospheric paths from the telescope to the shower. The results for EUSO-SPB1 are then compared with the expectations from previous analyses performed for EUSO-SPB1, based on both measurements and simulations. In addition, the paper provides an estimate of the expected detection rates for EUSO-TA. Both analyses have been performed via simulations of EUSO-TA with its own internal trigger algorithm and different electronics configurations, observing showers with different energy, direction, and impact point on the ground. The results are then compared to the real measurements, in which showers were identified by the external trigger from the TA-BRM-FDs.

2. The EUSO-TA detector

The EUSO-TA detector consists of an optical system with two flat Fresnel lenses of 1 m diameter and 8 mm thickness, made of Poly(methyl methacrylate) - PMMA [11]. The EUSO-TA focal surface has a concave shape, size of about 17 cm × 17 cm, and consists of an array of 3 × 3 Elementary Cells (ECs), each one made of 2 × 2 Hamamatsu Multi-Anode Photo-Multiplier Tubes (MAPMTs, model R11265-M64) [12]. The array of 6 × 6 MAPMTs and the readout electronics make the so called Photo-Detection Module (PDM). A Fresnel lens and the PDM of the EUSO-TA detector are shown in Fig. 2. Each MAPMT has 8 × 8 pixels of 2.88 mm side and with a field of view (FOV) of $0.2^\circ \times 0.2^\circ$, which represents the angular resolution of the detector; the complete focal surface has 2304 pixels, and the total FOV of the detector is $\sim 10.6^\circ \times 10.6^\circ$. Each pixel has a gain (electron multiplication ratio) of more than 10^6, which allows single-photon counting and an overall photo-detection efficiency of ∼30%. A 2 mm thick UV band-pass filter (in the range 290–430 nm), made of BG3 material and with anti-reflective coating, is glued on top of each MAPMT.

The time resolution of most of the JEM-EUSO instruments is 2.5 μs, which was defined for the observations from space.[1] The readout is performed by one 64-channel SPACIROC1 ASIC chip [16] per MAPMT, with a dead time at the beginning of each GTU of 200 ns and 30 ns double pulse resolution.

As typical of fluorescence detectors, EUSO-TA works at nighttime and in the best cases in clear sky conditions, to reduce the effects of atmospheric and cloud attenuation. The elevation of the telescope axis can be manually changed from 0° to 30° above the horizon, whereas its azimuth is fixed at 53° from North counterclockwise, pointing to the CLF.

Data discussed in this paper have been acquired with the external trigger from the TA-BRM-FDs: in case of a trigger, a packet of 128 frames centered at the time of the trigger is saved. However, as the FOV of the TA-BRM-FDs is about 30 times that of EUSO-TA, not all the showers detected by the TA-BRM-FDs are inside the FOV of EUSO-TA. This issue is overcome thanks to the support of the Telescope Array Collaboration that provides us the list of showers inside the FOV of EUSO-TA. This does not guarantee that the same event is visible in the EUSO-TA data, as the sensitivities of the two experiments are different and also because the EUSO-TA observes only a portion of the shower, due to its small FOV, and therefore EUSO-TA might measure only a faint emission that cannot be distinguished from the background. For this reason, offline analysis is required to search for shower events in the EUSO-TA data. Moreover, the Telescope Array Collaboration performs the shower reconstruction and shares with the EUSO-TA group information about the showers that cross the FOV of EUSO-TA, such as the arrival time, direction, impact point on ground (also called "shower core position"), and energy, which can be used for further analyses.

The EUSO-TA experiment provides the opportunity to easily test the technology for existing and future experiments within the JEM-EUSO program, as it allows stable field observations for extended periods. To increase the quantity and quality of data acquisitions, an upgrade of the detector is foreseen, as discussed in Section 2.1.

2.1. Upgrade of EUSO-TA: EUSO-TA2

Up to now, data acquisition sessions were performed in parallel to those of the Telescope Array, taking advantage of the external trigger made available by the TA-BRM-FDs, optimized for the observation of UHECRs from ground. An upgrade of EUSO-TA is ongoing, to allow operations with upgraded electronics and self-trigger capability, defining the so-called EUSO-TA2 experiment.

The electronics will be upgraded with the installation of the new SPACIROC3 boards [17], with a dead time at the beginning of the GTU of 50 ns (instead of 200 ns) and 5 ns double pulse resolution (instead of 30 ns for SPACIROC1). This increases the sensitivity of the detector, in particular to close showers. Indeed, for these showers the flux of photons arriving on each pixel is higher than for distant showers, and moreover, the shower itself crosses the pixel FOV in short timescales. Reducing the time window in which single photons can be collected reduces the probability that more than one photon arrives in the same time window, which would result in the collection of the first photon and the loss of the following ones.

[1] The GTU of 2.5 μs corresponds to the time needed for an EAS-generated signal to cross, at the speed of light, the field of view of a pixel of a space-based detector observing a square area on ground of diagonal 750 km. This was kept also for the ground-based EUSO-TA, the first balloon-based EUSO-Balloon [13] and EUSO-SPB1 [14], in order to test the original design of a future space-based detector. It was reduced to 1 μs for the most recent balloon-based experiment EUSO-SPB2 [15], to operate a mission with a more appropriate time resolution for observations from the stratosphere.

Fig. 1. The EUSO-TA detector in front of the Black Rock Mesa Fluorescence Detector station.

The detector will also be upgraded with advanced self-triggering capabilities (level-1 trigger logic) [18]. This will be achieved by replacing the current PDM data processing board with a new board with more memory and resources, based on the system-on-chip Zynq XC7Z030 FPGA [19]. The data read-out will be possible on three timescales: 2.5 μs (D1-GTU) for the observation of showers (the basic time resolution of the JEM-EUSO detectors); 320 μs (D2-GTU = 128×2.5 μs) to follow the evolution of fast atmospheric events such as transient luminous events and lightning; and 40.96 ms (D3-GTU = $128 \times 128 \times 2.5$ μs) for slow events such as meteors and strange quark matter (strangelets). D1 and D2 data will be subject to two dedicated trigger logics (level-1 and level-2, respectively), while D3 data will be collected continuously and events will be recognized with offline event search algorithms.

The general idea of the level-1 trigger logic for shower detection with EUSO-TA is to select pixels with an excess of counts/pixel over an adaptive threshold, which is independent for each pixel. When the number of pixels with counts above threshold is higher than a preset value, a trigger signal is transmitted. The procedure to set an independent threshold for each pixel consists first in computing the average counts for each pixel every 128 GTUs, comprising basically just the background photons. Then, an adaptive threshold of 4 σ above the background is set for the following 128 GTUs (where σ^2 is the variance of the Poisson-distributed background). Every pixel has its independent threshold to take into account the different backgrounds inside the FOV and also the different responses of the pixels. There are several requirements on the number, the spatial and temporal distributions of pixels above threshold to be able to detect both close/faint and distant/bright showers. For example, a low-energy shower close to the detector will produce a fast and faint signal on a large portion of the PDM, while a more distant shower will produce a track that will persist on the same MAPMT for a few GTUs. Therefore, the check of the pixels above threshold is done at the MAPMT, EC, and PDM level and for 1 GTU and 2 consecutive GTUs.

In Section 4.2, analyses of simulations using the level-1 trigger are discussed, in order to estimate the detection limit of EUSO-TA. Moreover, in Section 4.4, a study to evaluate the level-1 trigger rates via simulations is reported. Both analyses include a comparison of the trigger performance with the SPACIROC1 and SPACIROC3 ASIC boards, different elevations of EUSO-TA, and two background levels.

3. Observation of UHECR events

Four data acquisition sessions in 2015 (excluding the first one dedicated to set up the detector and to perform the first tests) and one in 2016 (devoted to test the EUSO-SPB1 performance before the launch) were done using externally extracted shower triggers from

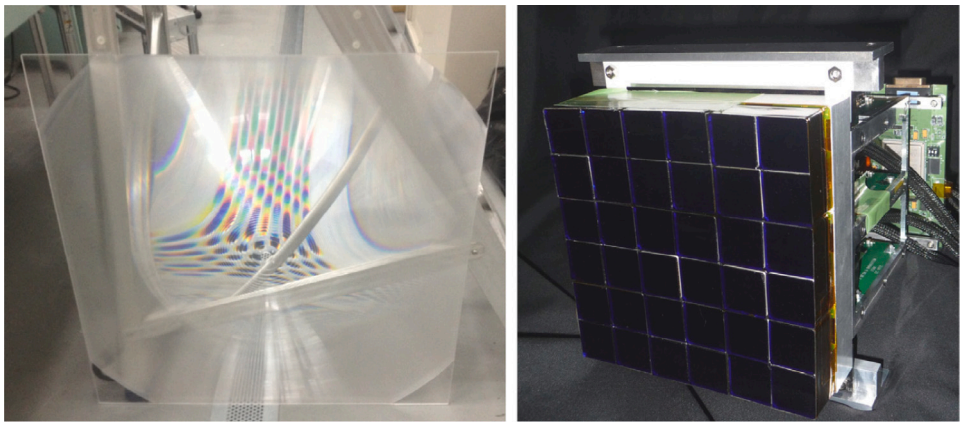

Fig. 2. A Fresnel lens of the EUSO-TA optical system (left) and the PDM composed by a focal surface with 6 × 6 MAPMTs and electronics boards behind it (right). *Source:* Photos taken from [4].

the TA-BRM-FDs, which we call external triggers, for a total of about 140 h. One acquisition session is normally a few days of acquisitions during nighttime, in clear sky conditions, and with no or low Moon illumination. The analysis reported in this paper uses data taken in 2015, equivalent to approximately 123 h.

As the FOV of TA-BRM-FDs includes the EUSO-TA one, the TA-BRM-FDs detect all the showers in the EUSO-TA FOV. The Telescope Array Collaboration provided a list of 110 showers that crossed the EUSO-TA FOV during its acquisition time. Nine of them have been identified in the EUSO-TA data as shower tracks visible above background at the expected time (parameters of these showers are in Table A.5), while 83 were not. The remaining 18 showers were discarded from the analysis because, based on the Telescope Array Collaboration analysis, the shower tracks were just on the edge of the EUSO-TA FOV or crossed malfunctioning MAPMTs, making the identification of the events very difficult or impossible. Moreover, although a few events look bright as seen by the TA-BRM-FDs, they were not found in the EUSO-TA data. A possible reason is that EUSO-TA works in single-photon counting mode with a time resolution of 2.5 μs, which is a technique designed for observations from space, while TA-BRM-FDs operate with a time resolution of 100 ns. The GTU is pretty large for observations on ground, therefore a lot of background photons are collected compared to those from fast-moving shower tracks that arrive on the same pixel in a few tens of nanoseconds, depending on the distance. Furthermore, some events might have occurred during the dead time of EUSO-TA.

The Telescope Array Collaboration also provided the reconstruction parameters of the showers, reconstructed in monocular mode (using just data collected with the TA-BRM-FDs). These parameters comprise the impact parameter R_p, i.e. the shortest distance between the shower axis and the detector in the shower-detector plane; the reconstructed energy of the primary particle E_{recTA}; the coordinates of the shower core; and the zenith and azimuth angles of the shower axis.

In Fig. 3 both the detected and the non-detected events are presented in an impact parameter vs. reconstructed energy plot. The typical uncertainty on the energy corresponds to that of the reconstructed energy by the Telescope Array Collaboration [20] in monocular mode, equal to the 17% of the reconstructed energy, and the error bars are within the marker size. The showers detected by EUSO-TA have high energy as they generate bright events that could be recognized over the background. Indeed, the EUSO-TA design is optimized for space-based observations, while TA was developed for observations from the ground, making it possible to detect showers with lower energies, which are invisible in the EUSO-TA data, although they cross its FOV. The spatial resolution is higher for EUSO-TA than for the TA-BRM-FDs, which is ∼0.2° for the first and 1° for the latter. As the FOV of the TA-BRM-FDs covers 33° in elevation and 108° in azimuth, the event reconstruction is based on the observation of the whole or majority of

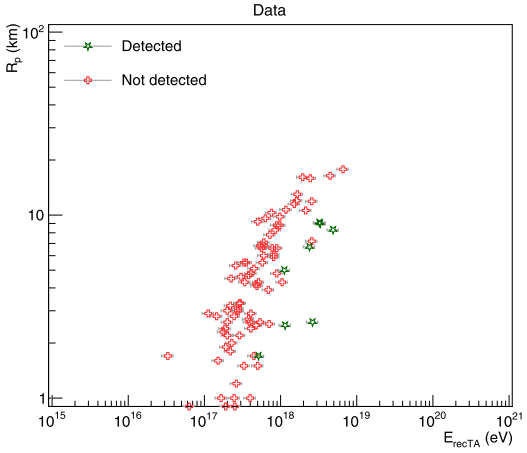

Fig. 3. Showers crossing the FOV of EUSO-TA with the impact parameter vs. the reconstructed energy provided by the Telescope Array Collaboration.

the shower, including the shower maximum, i.e. the point along the shower longitudinal axis with the maximum number of particles. From the reconstruction of the shower, it is possible to estimate the energy of the primary particle. On the other hand, EUSO-TA has a FOV of 10.6° × 10.6° in elevation and azimuth, which is, by construction, inside the FOV of the TA-BRM-FDs. This means that in the case of a shower in its FOV, EUSO-TA observes just a small portion of it, and in most cases it does not observe the maximum. This is not the case for space-based experiments, which observe the entire shower and for which the energy detection threshold is given by the number of photon counts coming from the maximum of the detected shower.

The plot on the top-left in Fig. 4 shows a shower detected by EUSO-TA in 1 GTU, and the color scale shows the counts/pixel/GTU. The same event is represented on a re-binned histogram on the top-right, where 4 × 4 original pixels are grouped in a pixel with comparable angular resolution to the TA-BRM-FDs one. A more precise choice 5 × 5 original pixels was avoided not to mix pixels of different MAPMTs, that might have different responses. Four MAPMTs were not working properly at the time of the observation. The plot on the bottom shows the same event detected by the TA-BRM-FDs, in which each circle represents one PMT of the TA-BRM-FDs, and the EUSO-TA FOV is indicated with a red rectangle.

The energy and distance of the showers crossing the FOV of EUSO-TA, whether detected or not, can be used to estimate the detection limit of EUSO-TA in terms of energy and distance to showers. To study this, it is necessary to consider that the detector observes only

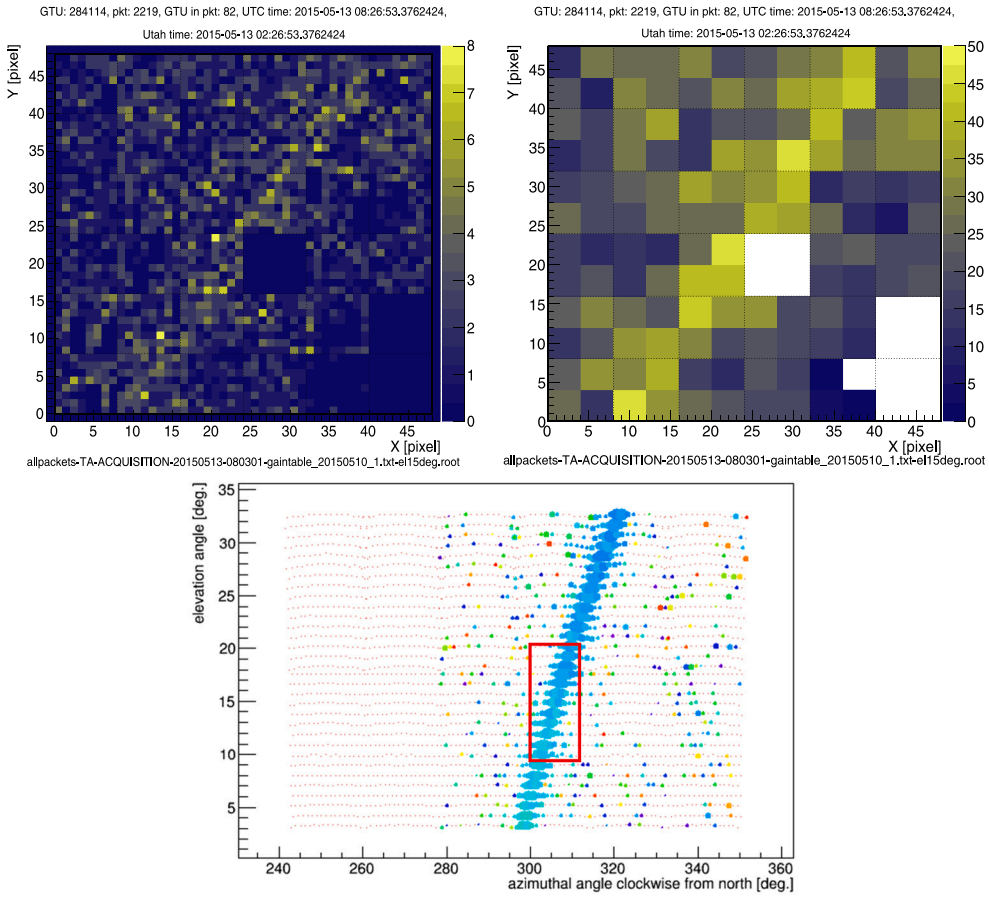

Fig. 4. The UHECR event detected on May 13th, 2015, with impact parameter $R_p = 2.5$ km and energy $E_{\mathrm{recTA}} = 1.15 \times 10^{18}$ eV. On the top-left, the event detected by EUSO-TA operating with and elevation angle 15°, showing the shower track in terms of counts/pixel/GTU. On the top-right, the same event is shown on a re-binned histogram reproducing a comparable angular resolution to the TA-BRM-FDs. At the top and the bottom, information about the time of the acquisition and filename is present, as shown by the ETOS software used to visualize and analyze data and simulations [21]. On the bottom, the same event detected by TA-BRM-FDs is shown, and each circle represents one PMT of the TA-BRM-FDs. The red frame indicates the FOV of EUSO-TA.

a portion of the shower, that might be far from the shower maximum. For this reason, the observed shower would look dimmer than the same shower observed at the maximum, and can be recognized only if its intensity is higher than the background. This requires the evaluation of an equivalent energy of the partially-observed shower that is lower than the real energy of the cosmic ray (see Section 4.1 for more details on the equivalent energy). Such an energy allows one to study the detection limit of the detector.

In the next sections, the analyses of the detected and undetected events performed on both simulation sets and data are discussed.

4. Analysis of the detected and undetected events

4.1. Correction of the energy

As seen in Section 3, not all the events that were detected by the TA-BRM-FDs and crossed the EUSO-TA FOV have been found in the EUSO-TA data. One reason lies in the fact that EUSO-TA observes only a portion of the showers, and the corresponding light intensity is lower than that of the same shower observed at the maximum. As the light intensity is proportional to the energy of the shower, it is possible to associate the observation made with EUSO-TA to a fictitious energy as if the shower was observed at the maximum, and this energy is the aforementioned equivalent energy. In this section, a method to compute the equivalent energy is provided.

4.1.1. Equivalent energy of the shower in the FOV

To estimate the equivalent energy E_{eq} of the section of shower crossing the EUSO-TA FOV, which is generally lower than the energy estimated when the entire shower is observed, including its maximum, an energy conversion factor has to be calculated and applied to the real energy of the shower. The real energy E_{real} is the reconstructed energy from the Telescope Array Collaboration E_{recTA} in case of real data, or the simulated energy in case of simulations E_{sim}.

On the left of Fig. 5, a scheme of the simultaneous observation of a shower by EUSO-TA and TA-BRM-FDs is shown. While the TA-BRM-FDs observe most of the shower development that includes the maximum emission of particles at the atmospheric depth X_{max}, EUSO-TA observes only a portion of it. The vertical atmospheric depth is the thickness of the air from the ground level up to the top of the atmosphere and is measured in $\mathrm{g/cm^2}$. Here, as is conventionally done, we use the slant depth, or the depth measured along the shower axis. In Section 4.1.2 there will be a distinction between vertical and slant depth. In Fig. 5, EUSO-TA observes above the maximum, though in general this depends on the distance of the shower from the detector, its elevation angle, and the energy and the zenith angle of the shower. It is visible that the portion of the shower observed by EUSO-TA is smaller than that observed by TA-BRM-FDs. Therefore, assuming that the major contribution to the energy reconstruction with fluorescence detectors is given by the energy loss at the shower maximum, it is possible to estimate, with simulations, the energy of a fictitious shower based on

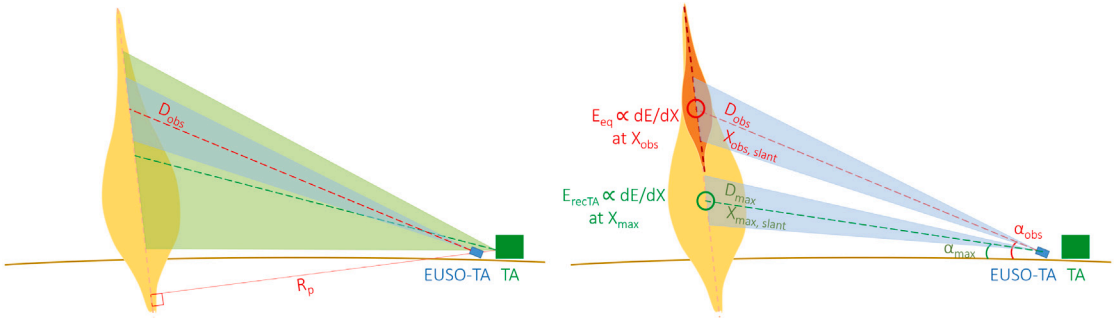

Fig. 5. On the left, a schematic view of a shower (shaped in yellow) in the FOV of the TA-BRM-FDs (in green) and in the smaller FOV of EUSO-TA (in blue). On the right, EUSO-TA observing the portion of the shower during a measurement (center of the FOV in the red circle) and pointing artificially to the shower maximum (center of the FOV in the green circle). The equivalent energy of the observed portion of the shower is ideally that of the less energetic shower inside the FOV during the observation (with a thinner profile in orange).

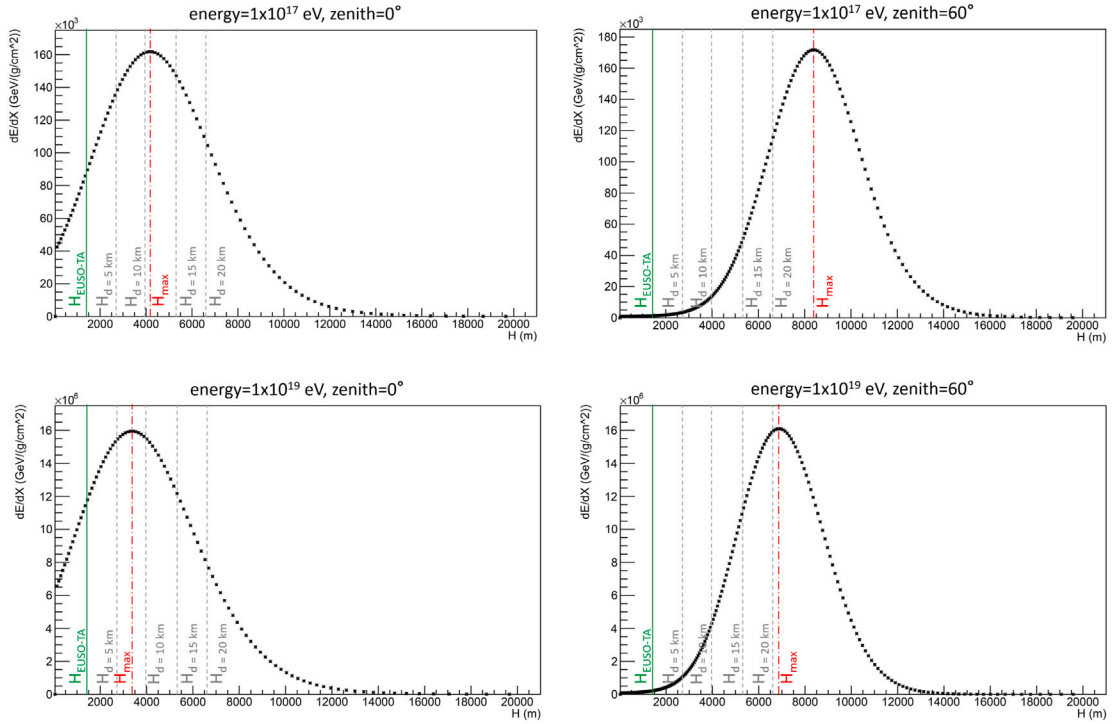

Fig. 6. Longitudinal shower profiles from CONEX simulations. They represent the energy loss dE/dX vs. the altitude H for showers with energy 1×10^{17} eV (top) and 1×10^{19} eV (bottom); with zenith angle 0° (left) and 60° (right). Vertical lines indicate the altitude of the EUSO-TA site at 1400 m a.s.l. in green, the altitude at which there is the maximum of the shower in red, and the altitude at which EUSO-TA, with a fixed elevation angle of 15°, observes the same shower placed at fixed distances measured along the optical axis: 5, 10, 15, and 20 km.

the energy loss from the observed portion of the shower at $X_{\rm obs}$, as depicted in Fig. 5 on the right. Such estimation can be performed by applying a conversion factor to the real energy of the shower.

To calculate the conversion factors, shower simulations have been performed with CONEX [22], with the QGSJETII-04 hadronic interaction model [23]. These simulations provide the distribution of the energy loss (proportional to the number of generated particles) with respect to the altitude. In Fig. 6 four proton shower profiles are reported, as an example. They represent the energy loss dE/dX versus the altitude H for showers with energy 1×10^{17} eV at the top and 1×10^{19} eV at the bottom, and with zenith angle 0° on the left and 60° on the right. The energy loss profiles vary depending on the energy and the zenith angle of the shower. Indeed, the shower maximum is at higher altitudes for low energies – as fewer particles are produced and the energy is spread earlier among them; and for high zenith angles – as the shower crosses a longer path in the atmosphere and loses energy higher in the atmosphere. Therefore, low-energy and inclined showers develop higher in the atmosphere than the more energetic and vertical showers. All the plots have a green line at the altitude of the EUSO-TA site $H_{\rm EUSO-TA}$, which is about 1400 m above sea level, and a red line at the altitude of the shower maximum $H_{\rm max}$. The gray lines are drawn at the altitude of the intersection point between the EUSO-TA optical axis (with an elevation of 15°, in this case), and the shower axis, observed at fixed distances measured along the optical axis. The chosen distances are 5, 10, 15, and 20 km, covering the range of distances involved in the measurements, and are reported next to each gray line. The plots demonstrate that the altitude at which EUSO-TA observes the shower can be both above and below the maximum, depending on the distance.

To compute the energy conversion factors, CONEX simulations were performed to reproduce shower profiles with several energies ($E = 1\times10^{17} - 1\times10^{20}$ eV, with steps of $\log E\,(\rm eV) = 0.1$) and zenith angles (θ =0°–65°, with steps of 5°). The longitudinal development of the shower does not depend on the azimuth angle, so only showers with azimuth angle 0° were simulated. Several elevation angles of EUSO-TA

(10°, 15°, 20°, and 25°) and distances from the detector (D = 1–50 km, in steps of 1 km) were considered. Combinations of distance, energy, and direction of the showers, and of the EUSO-TA elevation angle, make it possible to find points in the energy loss distribution corresponding to the center of the FOV during a shower observation and to the shower maximum. Both proton and iron were used as primary cosmic rays in the CONEX simulations.

The energy conversion factor is the ratio between the energy loss of the shower at the observed point (at the center of the FOV) and the energy loss at the shower maximum:

$$f_{\mathrm{E}} = \frac{(\mathrm{d}E/\mathrm{d}X)_{\mathrm{obs}}}{(\mathrm{d}E/\mathrm{d}X)_{\mathrm{max}}}. \tag{1}$$

To reduce fluctuations in the results, 20 showers were simulated with each combination of energy and zenith angle. For each simulated shower, the conversion factors were calculated for different distances and elevation angles of EUSO-TA. Afterward, for each energy, zenith angle, and distance of the showers, and elevation angle of EUSO-TA, the average of the 20 conversion factors $\bar{f}_{\mathrm{E}}$ were tabulated, together with the average atmospheric depth and altitude of the shower maximum, $\bar{X}_{\mathrm{max}}$ and $\bar{H}_{\mathrm{max}}$, respectively. In parallel, for each set of 20 showers, the standard deviation of the mean was calculated and tabulated as the uncertainty of the conversion factors. Knowing the characteristics of the showers detected by EUSO-TA with the TA-BRM-FDs external trigger or the simulated ones that crossed the FOV of EUSO-TA (energy, zenith and azimuth angles, and impact point on ground), and the elevation angle of the detector, it was possible to refer to the corresponding (average) conversion factor and its uncertainty on an event-by-event basis. In the case of intermediate values of the shower parameters with respect to those tabulated, an interpolation between different conversion factors was made, in order to find a more accurate one. The energy conversion factor is <1 if the observed part of the shower is above or below the maximum, or 1 in case the maximum was inside the FOV. The equivalent energy can be calculated by multiplying the real energy (reconstructed by Telescope Array in case of real data, or simulated in case of simulations) and the conversion factor:

$$E_{\mathrm{eq}} = f_{\mathrm{E}} \cdot E_{\mathrm{real}}. \tag{2}$$

The values of the energy conversion factors for protons with several combinations of (real) energy and zenith angle of the shower, distance from the detector and elevation angle of the detector are displayed in Fig. 7. The plots refer to elevation angles of 10°, 15°, 20°, and 25° (from top to bottom), and zenith angles of 0°, 30°, and 60° (from left to right). The central part of the yellowish bands with high values of the conversion factors (very close to 1), represent the maxima of the showers, and bluish areas correspond to lower conversion factors, and therefore to portions of the showers far from their maxima. As expected, by increasing the energy and reducing the zenith angle, the maximum of the showers is at lower distances from the detector, i.e. lower altitudes. By varying the elevation angle of the detector, different portions of the showers are observed, and therefore the conversion factors change accordingly. Plots of the conversion factors considering iron as primary are visible in Fig. B.18. As showers from iron primaries have the maximum at ∼100 g/cm^2 lower than showers from protons, i.e. at higher altitudes, the values of the conversion factors for iron reflect this trend, with the yellowish bands at longer distance than those for protons.

An example of a simulation of a shower detected with EUSO-TA with the pre-defined elevation angle and when pointing to the shower maximum is depicted in Fig. 8. The shower has an energy of 4.68×10^{18} eV, a zenith angle of 56.4°, and an azimuth angle of 141.9°, moving towards EUSO-TA. The distance of the shower to the detector, measured inside its FOV, with the pre-defined elevation angle of 10°, is 6.7 km. To point to the shower maximum, whose altitude is retrieved from the simulation, an elevation angle of 22.75° is required, and the distance becomes 10.0 km. The image on the left side represents the shower observed with the elevation angle of 10°, while that on the right side represents the same shower observed at the maximum at 22.7°. Therefore, the energy of $4.68{\times}10^{18}$ eV corresponds approximately to the shower track observed when pointing at the maximum, while the energy of the observed portion of the shower under the maximum should correspond at a lower energy. The energy conversion factor for this shower is $f_{\mathrm{E}} = 0.101 \pm 0.011$, therefore the equivalent energy of the observed portion of the shower is $(0.101 \pm 0.011) \times 4.68 \times 10^{18} = (4.77 \pm 0.49) \times 10^{17}$ eV.

Further corrections to take into account the atmospheric effects on the shower detection are discussed in the next section.

4.1.2. Atmospheric transmission

The atmospheric transmission depends on the thickness of atmosphere crossed by photons and has to be taken into account for the estimation of the energy of the observed portion of the shower. Indeed, the slant depth along the EUSO-TA optical axis pointing to the shower with a pre-defined elevation angle is different from that pointing to the shower maximum (see the sketch on the right side of Fig. 5). Both Rayleigh and Mie scattering are taken into account. The first occurs when the dimensions of the scattering center is much smaller than the wavelength of the incident photons (atoms and molecules), and vice-versa for the latter (aerosol particles).

In this analysis, to correct the energy of the showers for the Rayleigh scattering, the Linsley parametrization used in the CORSIKA simulation software [24] is considered to retrieve the atmospheric depths at given altitudes, taking into account that the atmospheric density varies with the altitude. For a given atmospheric depth X, the atmospheric transmission is given by

$$T^{R} = \exp\left(-\frac{X}{\Lambda(\lambda)}\right), \tag{3}$$

where $\Lambda(\lambda)$ is the mean free path of photons due to Rayleigh scattering and depends on the photon wavelength. Since the wavelength range of interest is the near-UV, in this analysis Λ(350 nm) = 1700 g/cm^2 [25] was used as 350 nm is close to both the mean value of the bandwidth of the BG3 filter (280–430) nm and the main peak of the fluorescence spectrum (∼351.5 nm) [26]. The atmospheric slant depth-integrated along the telescope axis up to the observed point of the shower can be calculated as:

$$X_{\mathrm{obs}}^{\mathrm{slant}} = \frac{\left(X_{\mathrm{ground}}^{\mathrm{vertical}} - X_{\mathrm{obs}}^{\mathrm{vertical}}\right)}{\sin\alpha_{\mathrm{obs}}}, \tag{4}$$

and the one integrated up to the shower maximum as:

$$X_{\mathrm{max}}^{\mathrm{slant}} = \frac{\left(X_{\mathrm{ground}}^{\mathrm{vertical}} - X_{\mathrm{max}}^{\mathrm{vertical}}\right)}{\sin\alpha_{\mathrm{max}}}, \tag{5}$$

where $X_{\mathrm{ground}}^{\mathrm{vertical}}$ and $X_{\mathrm{max}}^{\mathrm{vertical}}$ are the atmospheric vertical depths at the altitude of the EUSO-TA site and at the altitude of the shower maximum, respectively; and α_{obs} and α_{max} are the elevation angles used during the observation and when pointing to the maximum, respectively. Therefore, the atmospheric transmission $T_{\mathrm{obs}}^{\mathrm{R}}$ corresponding to the atmospheric slant depth $X_{\mathrm{obs}}^{\mathrm{slant}}$ is:

$$T_{\mathrm{obs}}^{\mathrm{R}} = \exp\left(-\frac{X_{\mathrm{obs}}^{\mathrm{slant}}}{\Lambda(350\,\mathrm{nm})}\right), \tag{6}$$

and the atmospheric transmission T_{max} considering the atmospheric slant depth at the maximum $X_{\mathrm{max}}^{\mathrm{slant}}$ is:

$$T_{\mathrm{max}}^{\mathrm{R}} = \exp\left(-\frac{X_{\mathrm{max}}^{\mathrm{slant}}}{\Lambda(350\,\mathrm{nm})}\right). \tag{7}$$

To calculate the atmospheric transmission considering the aerosol scattering, the vertical aerosol optical depth $\tau_{\mathrm{aer}}^{\mathrm{TA}}(5\ \mathrm{km})$ measured at 5 km above the ground at the TA site were used [27]. They increase with the altitude until they become almost constant at 5 km altitude,

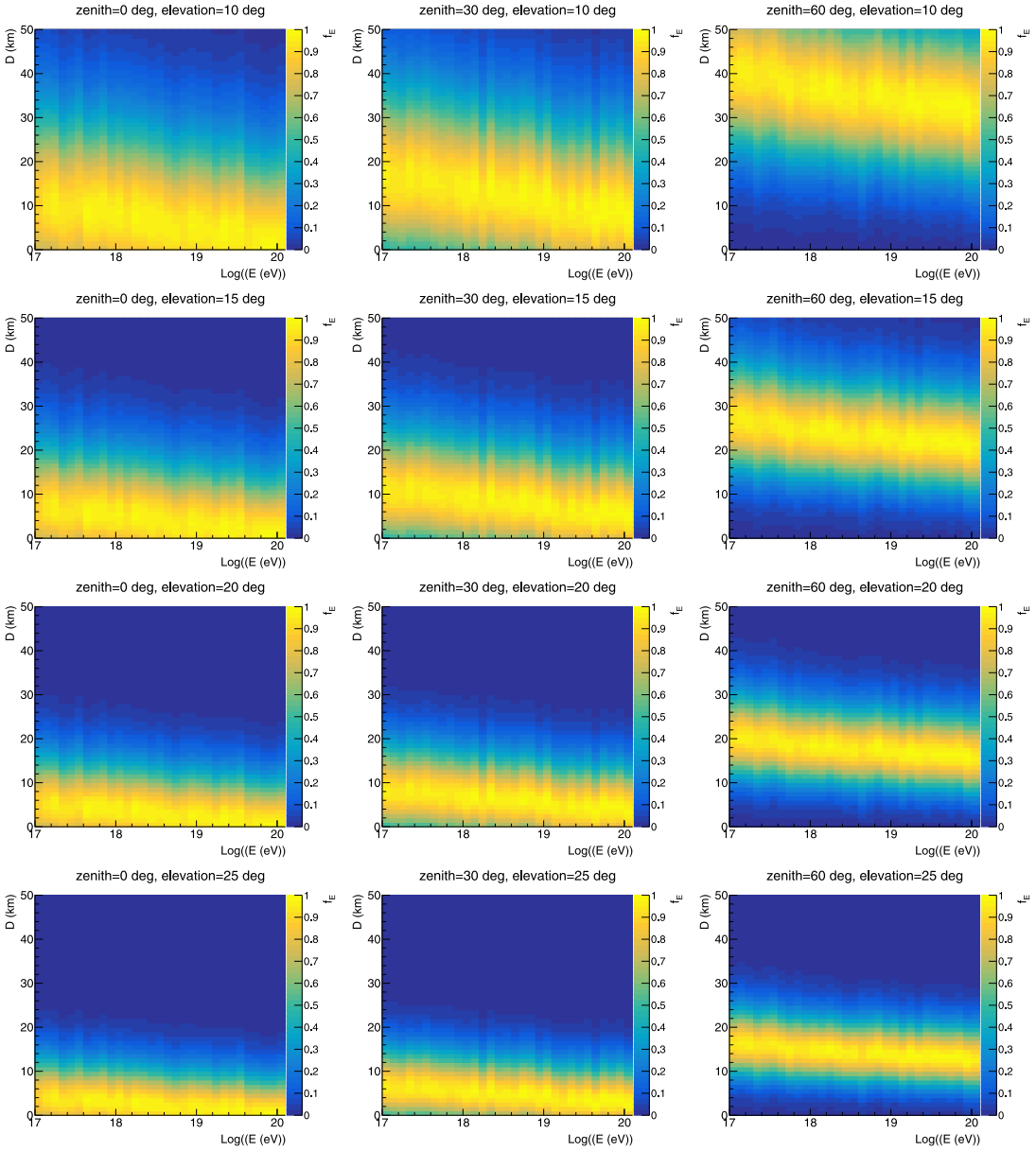

Fig. 7. Energy conversion factors for proton primaries as a function of the shower energy and distance from the detector. The plots refer to 10°, 15°, 20°, and 25° elevation angles and 0°, 30°, and 60° zenith angles.

where the presence of aerosol is negligible. They are subject to seasonal variation, indeed the measurements performed at the TA site have a monthly frequency. Since most EUSO-TA shower observations are below 5 km altitude, the $\tau^{\mathrm{TA}}_{\mathrm{aer}}(5\ \mathrm{km})$ has to be rescaled. The dependency of $\tau^{\mathrm{PAO}}_{\mathrm{aer}}(h)$ on the height h, measured at the Pierre Auger Observatory (PAO) and available in [28] were used for this, and then rescaled to the values measured at the TA site. In general, the vertical aerosol optical depth can be expressed as the integral over the height of the aerosol extinction $\epsilon_{\mathrm{aer}}(h)$, whose dependency on the height is:

$$\epsilon_{\mathrm{aer}}(h) = \frac{1}{L_{\mathrm{aer}}} \cdot \exp\left(-\frac{h}{H_{\mathrm{aer}}}\right), \tag{8}$$

where L_{aer} and H_{aer} are the aerosol horizontal attenuation length and the aerosol scale height, respectively. Therefore, the vertical aerosol optical depth becomes:

$$\tau_{\mathrm{aer}}(h) = -\frac{H_{\mathrm{aer}}}{L_{\mathrm{aer}}} \cdot \left[\exp\left(-\frac{h}{H_{\mathrm{aer}}}\right) - 1\right]. \tag{9}$$

The values of $\tau^{PAO}_{aer}(h)$ from the simulation study performed in conditions of high, average, and low aerosol attenuation have been fitted with a function like the one above, to retrieve the parameters H_{aer} and L_{aer}. The $\tau^{TA}_{\mathrm{aer}}(h)$ for any height was calculated as:

$$\tau^{\mathrm{TA}}_{\mathrm{aer}}(h) = \frac{\tau^{\mathrm{PAO}}_{\mathrm{aer}}(h)}{\tau^{\mathrm{PAO}}_{\mathrm{aer}}(5\ \mathrm{km})} \cdot \tau^{\mathrm{TA}}_{\mathrm{aer}}(5\ \mathrm{km}). \tag{10}$$

The transmission along the direction of observation considering the Mie scattering by the aerosol particles can be calculated as:

$$T^{\mathrm{M}} = \exp\left(-\frac{\tau^{\mathrm{TA}}_{\mathrm{aer}}(h)}{\sin\alpha}\right), \tag{11}$$

where α is the elevation angle of EUSO-TA. Thus, with the same procedure used for the Rayleigh scattering, the atmospheric transmission along the observation direction and when pointing at the shower maximum are:

$$T^{\mathrm{M}}_{\mathrm{obs}} = \exp\left(-\frac{\tau^{\mathrm{TA}}_{\mathrm{aer}}(h)}{\sin\alpha_{\mathrm{obs}}}\right), \tag{12}$$

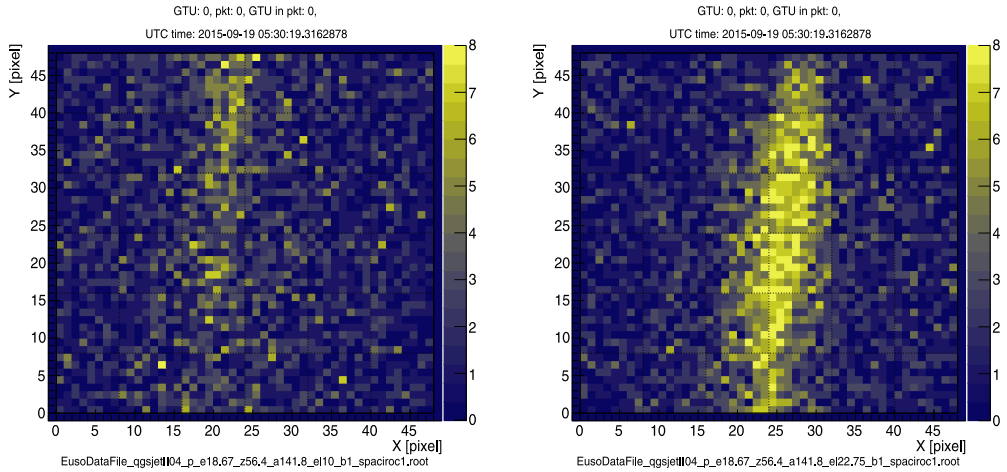

Fig. 8. The same simulated shower with energy 4.68×10^{18} eV, zenith angle 56.4° and azimuth angle 141.9° observed with an elevation angle of 10° (left) and pointing at the maximum of the shower with an elevation of 22.75° (right). Both images contain text giving information about the events, as shown by the ETOS software.

$$T^{\mathrm{M}}_{\mathrm{max}} = \exp\left(-\frac{\tau^{\mathrm{TA}}_{\mathrm{aer}}(h)}{\sin\alpha_{\mathrm{max}}}\right) \tag{13}$$

Moreover, as the number of photons arriving at the detector is inversely proportional to the square of the distance from their source, the atmospheric transmission has to be corrected also for this factor.

In a similar way to the method used for the calculation of the equivalent energy, the atmospheric correction factor f_{atm} is calculated as the ratio between the atmospheric transmission in the direction of observation and that pointing to the shower maximum, both corrected for the distance:

$$f_{\mathrm{atm}} = \frac{T^{R}_{\mathrm{obs}}}{T^{R}_{\mathrm{max}}} \cdot \frac{T^{M}_{\mathrm{obs}}}{T^{M}_{\mathrm{max}}} \cdot \frac{D^{2}_{\mathrm{max}}}{D^{2}_{\mathrm{obs}}}, \tag{14}$$

where D_{max} and D_{obs} are the distance to the shower maximum and to the observed portion of the shower, respectively. The atmospheric correction factor is in principle equal to 1 if EUSO-TA directly observes the shower maximum, but in general, it is greater or lower than 1, depending on the shower direction with respect to the detector and the elevation angle of the telescope. The equivalent energy corrected for the atmospheric transmission becomes therefore:

$$E_{\mathrm{eq,atm}} = f_{\mathrm{atm}} \cdot E_{\mathrm{eq}}. \tag{15}$$

4.2. Analysis of the simulated events

4.2.1. Simulation set

Two sets of 10 000 showers were produced via CONEX simulations, one with proton and one with iron primaries, with the QGSJETII-04 hadronic interaction model, zenith angles in the range 0°–90° drawn from the isotropic flux on a flat surface, i.e. $dN/d\cos(\theta) \sim \cos(\theta)$ and random azimuth angles in the range 0°–360°. The energy range was $1 \times 10^{17} - 1 \times 10^{20}$ eV and the spectral index for the energy distribution was initially −1 in order to have statistics also at the highest energies, but was properly rescaled afterward during the analysis to retrieve the spectral index −2. The CONEX showers were then processed with the Offline framework [29,30] to perform the production and propagation of fluorescence and Cherenkov photons from the shower to the detector through the atmosphere, and the detector response including the level-1 trigger, foreseen in the upgraded version of the detector. Offline generated the impact point on the ground of the showers on an area of $36 \times 28\,\mathrm{km}^2 = 1008\,\mathrm{km}^2$ centered at half the distance between EUSO-TA and the CLF. The elevation angles chosen for EUSO-TA were 10°, 15°, 20° and 25°, while the simulated background levels were 1 and 1.5 counts/pixel/GTU. The values of both the elevation angles and background levels were realistic, reproducing the conditions in which the real measurements were performed.

Among all the simulated showers, just a fraction of them actually enter the FOV of EUSO-TA, due to geometrical constraints. The ratio between the triggered showers and those that entered the FOV but were not triggered are plotted in Fig. 9. On the axes there are the coordinates in the Universal Transverse Mercator (UTM) system. Each plot represents showers within a range of energy in logarithmic scale $\log E$ (eV): top-left 18–18.5, top-right 18.5–19, bottom-left 19–19.5, bottom-right 19.5–20. Below these energies no triggered showers are present. The plots indicate how the showers can be detected as a function of the energy and the distance. In Fig. C.21 plots with the shower core positions split by energy, zenith and azimuth angle give an overview of the simulation setup.

4.2.2. Detection limit via analysis of the simulations

In Section 4.1 the methodology used to estimate the equivalent energy of the showers observed by EUSO-TA was described. Such energies can be analyzed to determine the detection threshold of the detector. This limit is important in general for the JEM-EUSO program, and in particular, can be extended to balloon-based experiments.

With simulations it is possible to reach higher statistics than with the real observations and therefore they can be used to study the detection limit. The simulation set described in Section 4.2.1 was used for this purpose. The same procedure to rescale the energy was applied also to the data and the results are discussed in Section 4.3.1.

A few quality cuts have been applied to the showers for the further analysis:

- only events with >50 counts in at least one GTU are shown, to reduce the number of non-triggered events (this selection does not exclude triggered showers);
- only showers with zenith angle <65° are included, as the energy conversion factors are available up to this value;
- only events with the shower axis in the FOV are considered, excluding those that produce only scattered photons in the FOV, since these would not correctly reflect the shower energy.

In Fig. 10 the simulated showers are plotted with their distance measured along the optical axis of EUSO-TA (D_{obs} in Fig. 5) and the simulated energy, for elevation angle of 10° (left) and 25° (right), background level of 1 count/pixel/GTU, and SPACIROC1 electronics board, without the cut on the number of counts. In Fig. 11 the simulated showers are plotted with their distance measured inside the FOV of EUSO-TA, and simulated energy (top), equivalent energy (middle), and equivalent energy corrected for the atmospheric transmission (bottom).

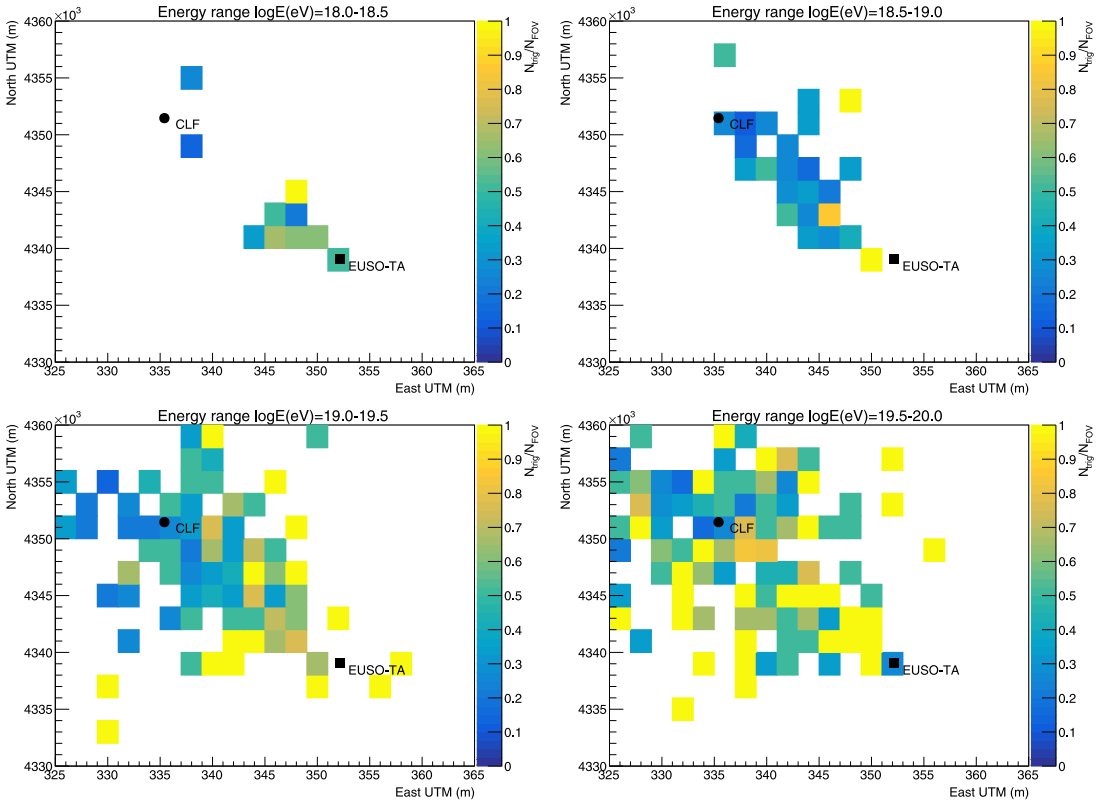

Fig. 9. Ratio between the triggered showers and those that entered the FOV but were not triggered, with the coordinates in the Universal Transverse Mercator (UTM) system. Simulations refer to proton showers and EUSO-TA elevation 15°. Each plot represents showers within a range of energy in logarithmic scale $\log E$ (eV): top-left 18−18.5, top-right 18.5−19, bottom-left 19−19.5, bottom-right 19.5−20. Markers for EUSO-TA and the CLF are placed as a reference.

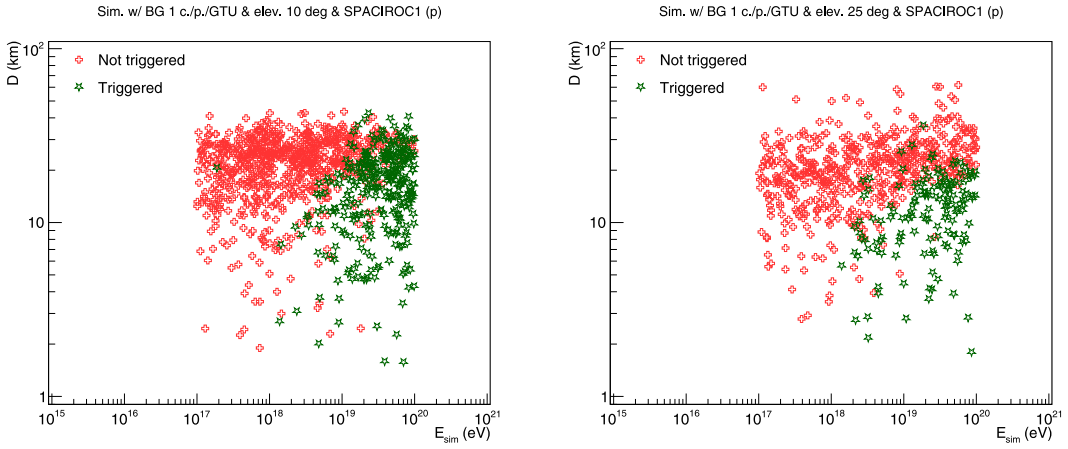

Fig. 10. Showers in the FOV and the triggered ones, represented with their distance to EUSO-TA and the simulated energy, for 10° (left) and 25° (right) elevation angle. The simulated background is 1 count/pixel/GTU and the electronic board version is SPACIROC1. No cuts on the number of counts are present.

In the bottom plots, the estimated EUSO-TA and EUSO-SPB1 detection limits are drawn as well, whose details will be described later in this section. Plots are for elevation angle of 10° (left) and 25° (right), background level of 1 count/pixel/GTU, and SPACIROC1 electronics board. The same analysis was performed also for the background level of 1.5 count/pixel/GTU, the intermediate elevation angles 15° and 20°, and SPACIROC3, but the corresponding plots are not shown in this paper for ease of reading.

Comparing the D vs. $E_{\rm sim}$ plots in Figs. 10 and 11, one can see that increasing the distance, only events with high energy generate >50 counts in at least one GTU. Moreover, at large distances more showers are selected by the cuts on the number of counts for elevation angle 10° rather than with 25°, and this is because increasing the elevation angle and the distance, the portion of a shower in the FOV is above the maximum where the number of emitted photons decreases.

The equivalent energy of each shower, which considers the portion of the shower inside the FOV (see Section 4.1.1), is generally smaller than $E_{\rm sim}$, as visible in the D vs. $E_{\rm eq}$ plots in the middle panels. The reason is that $E_{\rm eq}$ is lower than the $E_{\rm sim}$ when pointing above or below the shower maximum, and they are equal only when pointing exactly at the maximum. Also in this case there is a difference depending on the elevation angle: with elevation angle 25° it is more likely that the distant showers are observed above the maximum, and therefore there is a tail of events at larger distances, turning towards lower

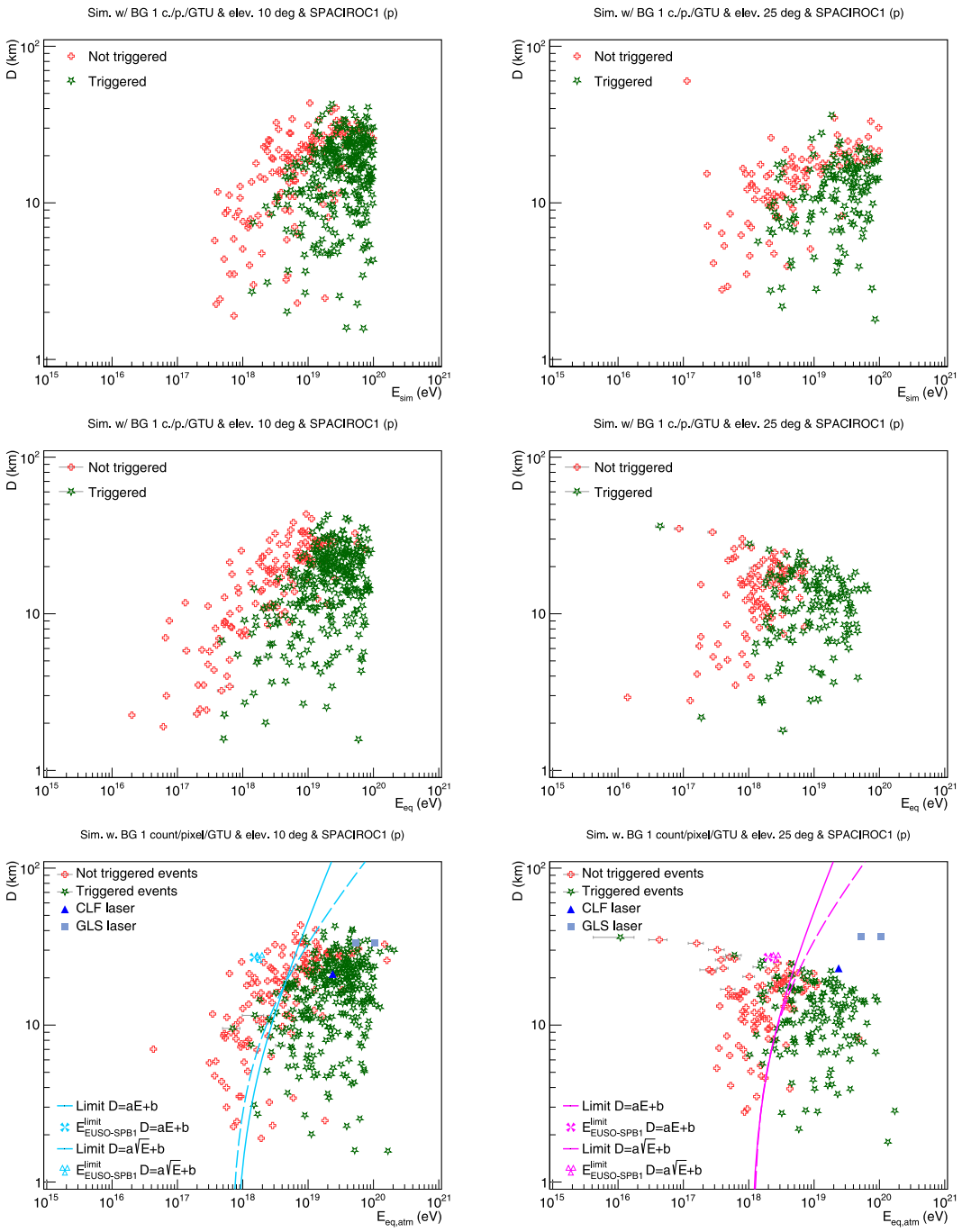

Fig. 11. Showers in the FOV and the triggered ones with number of counts >50, represented with their distance to EUSO-TA and the simulated energy (top), the equivalent energy (middle) and the equivalent energy corrected for the atmospheric transmission (bottom), for 10° (left) and 25° (right) elevation angle. The simulated background is 1 count/pixel/GTU and the electronic board version is SPACIROC1. In the bottom plots, the distance and energy of laser events generated by the CLF and the GLS system are shown, too. In the same plots, the evaluated EUSO-TA detection limits (for equations $D = aE + b$ and $D = a\sqrt{E} + b$) are drawn, as well as the corresponding limits of EUSO-SPB1. In the bottom-left plot, the energy limits of EUSO-SPB1 are overlapped.

equivalent energies. The distance at which this turn starts is ∼20 km, and it is visible also at intermediate elevation angles (15° and 20°). The uncertainty on the energy E_{eq} is the standard deviation of the mean of the conversion factors estimated for showers with the same characteristics and distance from EUSO-TA.

Finally, the equivalent energy of each shower is corrected for the atmospheric transmission (see Section 4.1.2), and the results are shown in the D vs. $E_{\mathrm{eq,atm}}$ plots in the bottom panels. In this case, $E_{\mathrm{eq,atm}}$ can be both smaller, equal, or greater than E_{eq}. The uncertainty on the energy $E_{\mathrm{eq,atm}}$ is the root sum square of the uncertainty on E_{eq} and the vertical aerosol optical depths measured by TA [27]. For reference, the distance and energy of laser events generated by the CLF and the GLS system during real measurements are shown, too. Such events were clearly visible above the background.

In Fig. 12 the atmospheric transmission affecting the observation of triggered and non-triggered showers is plotted with respect to the distance, for both 10° (left) and 25° (right) elevation angles. Increasing the elevation angle, the atmospheric transmission increases because the atmospheric thickness is less than when observing through the low atmosphere.

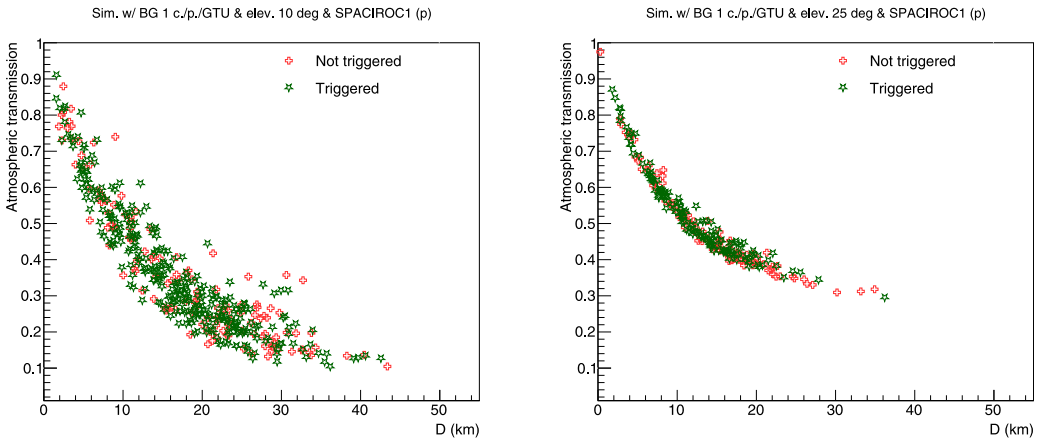

Fig. 12. The atmospheric transmission each shower is subjected to vs. its distance to EUSO-TA, for both the triggered and the non-triggered events. The plots are for both 10° (left) and 25° (right) elevation angles.

The D vs. $E_{\mathrm{eq,atm}}$ frame can be used to evaluate the detection limit of EUSO-TA. Such a limit should separate the triggered and the non-triggered events. However, they do partially overlap due to the variety of simulated showers, for the following reasons:

- Due to the variety of energies and directions simulated, showers with similar energy and distance but different orientations (zenith and/or azimuth angles) with respect to the detector might appear with different intensity, and therefore might be triggered or not. The orientation plays a main role concerning the Cherenkov emission, which is forward beamed along the shower axis.
- In the calculation of the equivalent energy, only the fluorescence emission is taken into account, proportional to the number of particles and the energy loss through the shower development that determines the longitudinal profile. Cherenkov emission is not considered. Therefore, depending on its direction, the shower might look brighter and generate more counts than those expected if only the fluorescence emission contributed to the signal. For this reason, showers with relatively low equivalent energy might overcome the cut on the counts and might be even triggered. For each simulated shower, in Fig. 13 the ratio between the total number of Cherenkov and the total number of fluorescence photons arriving at the detector is shown vs. the equivalent energy corrected for the atmospheric transmission. In general, the ratio is higher for elevation angle 10° (top-left) than 25° (top-right). Low ratios correspond to high distances (see later the description of the bottom plots). However, for a given corrected energy at which there are both triggered and non-triggered showers, the ratio tends to be higher for the first than the latter, indicating a role of the Cherenkov emission in the trigger response. The aforementioned ratio vs. distance indicates that the ratio decreases when the distance increases.
- Each shower profile simulated in this study might be different with respect to the average one (with the same parameters), used to calculate the energy correction factors and the atmospheric transmission factors, both based on the position of the average shower maximum. This is due to fluctuations from shower to shower, even those with the same energy, zenith and azimuth angles.

A set of simulations was made only with vertical showers, in order to exclude the effects due to the relative orientation between showers and detector, see Appendix D. In this case, the separation between triggered and non-triggered events is much clearer.

As the populations of triggered and non-triggered events are not simply separable, a method was defined to draw the detection limit of EUSO-TA. In principle, the triggered showers should lie on the right side of the detection limit (at higher energies), and the non-triggered ones on the left side. Therefore, one can define the efficiency of "properly" triggering the showers on the right side of the line and not triggering those on the left side of the line, as

$$\epsilon = \frac{N_{\mathrm{T}}^{\mathrm{right}} + N_{\mathrm{NT}}^{\mathrm{left}}}{N_{\mathrm{T}}^{\mathrm{tot}} + N_{\mathrm{NT}}^{\mathrm{tot}}}, \tag{16}$$

where $N_{\mathrm{T}}^{\mathrm{right}}$ and $N_{\mathrm{T}}^{\mathrm{tot}}$ are the number of triggered showers on the right side of the line and the total number of triggered showers, respectively, and, similarly, $N_{\mathrm{NT}}^{\mathrm{left}}$ and $N_{\mathrm{NT}}^{\mathrm{tot}}$ are the number of non-triggered showers on the left side of the line and the total number of non-triggered showers, respectively. The detection limit is approximated by finding the lines that maximize ϵ. With the purpose of extending the evaluation of the detection limit to balloon-based experiments, only showers with distance ≤20 km were considered in this part of the analysis, in order to avoid the influence of the tails of events at large distances whose equivalent energies are shifted back to low values because EUSO-TA observes them above the maximum. Indeed, this condition occurs during observations from ground, when the detector might point below, above, or at the maximum of the showers, while in the top-down perspective of detectors on balloons at a distance of ∼33 km, all or most of the shower development is inside the FOV.

As functions representing the limit, both the equations $D = a \cdot E + b$ and $D = a \cdot \sqrt{E} + b$ were considered, where D and E are the distance and the energy limit, respectively. The first equation takes into account that the longer the distance is, the longer the shower takes to cross the FOV of a pixel and, thus, the longer the counts are integrated in the same pixel. In this way, the energy limit has to be $E \propto D$, and vice-versa $D \propto E$. The second equation comes from the fact that the registered counts decrease as $1/D^2$ and that, therefore, the energy limit to register the minimum number of counts in order to trigger the shower has to be $E \propto D^2$, and vice-versa $D \propto \sqrt{E}$. The first equation is valid when the time needed by the shower to cross the FOV of a pixel is ≤1 GTU, i.e. at relatively short distances. When this time is >1 GTU, i.e. at larger distances, the signal starts to be split in different GTUs and therefore is lower in the sampling time of 1 GTU. At this point, the second equation starts to be more appropriate. However, it is not obvious how to define the distance at which there is the transition between the two trends, as the time needed by the shower to cross the FOV of a pixel is strongly related to its geometry.

Iterations over different values of the angular coefficient a and of the intercept b make it possible to find the lines that maximize ϵ, i.e. when most of the triggered showers are on the left side of the line and most of the non-triggered ones are on the right side of the line. That line corresponds to the detection limit. Table E.8 (for proton) and Table E.9 (for iron) in Appendix E reports the a and b parameters of

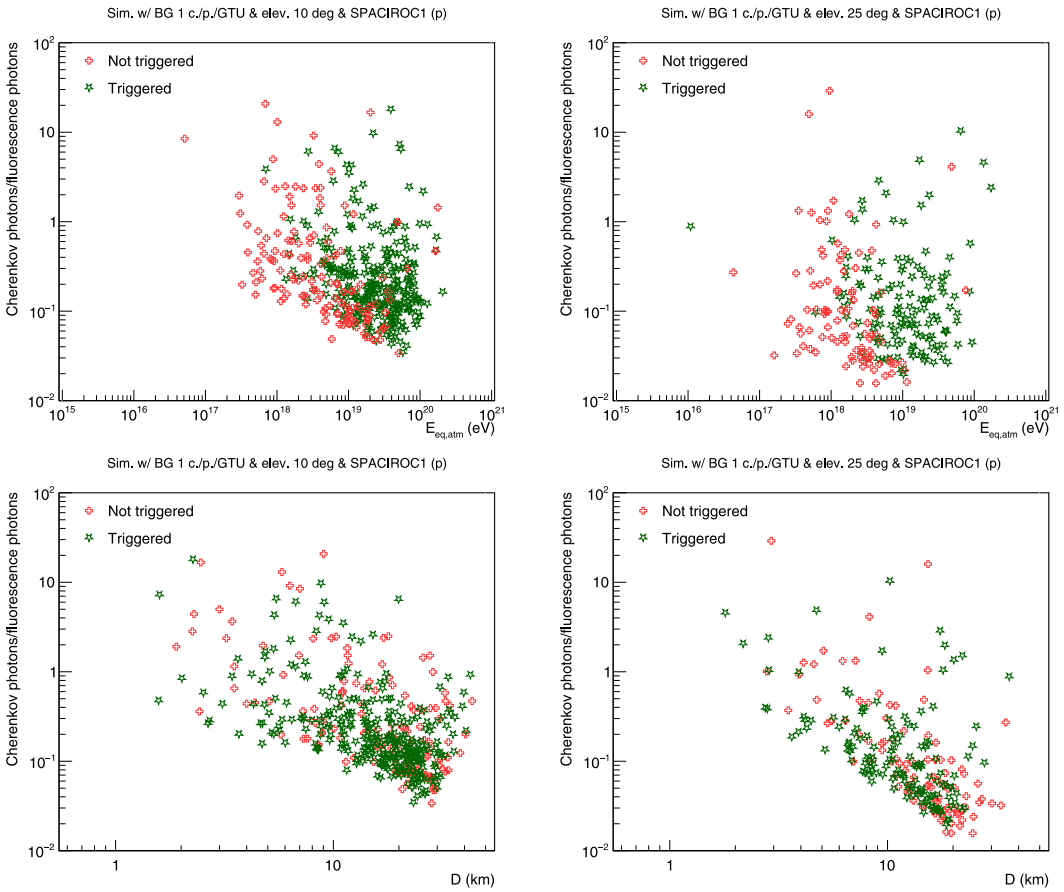

Fig. 13. The ratio between the total number of Cherenkov and fluorescence photons arriving at the detector vs. the equivalent energy corrected for the atmospheric transmission (top) and vs. the distance (bottom), for both the triggered and the non-triggered events. The plots are for both 10° (left) and 25° (right) elevation angles.

the lines representing the detection limits in the different background conditions (1 and 1.5 counts/pixel/GTU), elevation angles (10°, 15°, 20° and 25°), and with SPACIROC1 and SPACIROC3 electronics boards. Lines defining the detection limits for elevation angles 10° and 25° are drawn in the bottom plots in Fig. 11. The limits corresponding to all the elevation angles, the two background levels, and both the electronics boards are also displayed in Fig. 15, where they are overlayed with real measurements.

The detection limit of EUSO-TA can be preliminarily extended also for balloon-based experiments, as the distance of showers to the detector would be at most one order of magnitude larger than those observed with EUSO-TA. Although the results obtained for EUSO-TA should be scaled considering the different detection efficiency and atmospheric depth, this analysis still provides valuable information. This was done for EUSO-SPB1 that operated in 2017 at ~33 km altitude, and whose design was similar to the one of EUSO-TA (two Fresnel lenses and one PDM). In this analysis a distance of 27 km between EUSO-SPB1 and the maximum of a sample shower was considered, assuming that such a maximum was at 6 km altitude (see plots in Fig. 6). The overall detection efficiency of EUSO-TA was ~4.8% and that of EUSO-SPB1 was ~9.6% [31], measured with UV light sources during test campaigns. This means that, at the limit, EUSO-SPB1 could detect a shower with approximately half the energy of that detectable by EUSO-TA. However, EUSO-SPB1 could detect also two times the background photons as EUSO-TA in the same conditions. Therefore, the energy limit of EUSO-SPB1 can be evaluated as the energy limit of EUSO-TA at the same distance divided by $\sqrt{2}$. However, in order to compare the detection limits of the two experiments, it is necessary also to consider the different atmospheric depths between the detector and the showers, as EUSO-SPB1 observes them from nadir and EUSO-TA from the ground and with certain elevation angles. Similar to what discussed in Section 4.1.2, a correction factor for the atmospheric transmission $f_{\text{atm}}^{\text{slant/nadir}}$ was evaluated as the ratio between the atmospheric transmission for EUSO-TA along the slant depth $T_{\text{EUSO-TA}}^{\text{slant}}$ and that of EUSO-SPB1 pointing nadir $T_{\text{EUSO-SPB1}}^{\text{nadir}}$:

$$f_{\text{atm}}^{\text{slant/nadir}} = \frac{T_{\text{EUSO-TA}}^{\text{slant}}}{T_{\text{EUSO-SPB1}}^{\text{nadir}}}. \tag{17}$$

This ratio is <1, as the atmospheric depth is greater along inclined directions than vertical ones, and vice-versa for the atmospheric transmission (see Eqs. (4) and (6)). Therefore, if the energy limit for EUSO-TA at 27 km is $E_{\text{EUSO-TA}}^{\text{limit}}$ the energy limit for EUSO-SPB1 $E_{\text{EUSO-SPB1}}^{\text{limit}}$ becomes:

$$E_{\text{EUSO-SPB1}}^{\text{limit}} = f_{\text{atm}}^{\text{slant/nadir}} \cdot \frac{E_{\text{EUSO-TA}}^{\text{limit}}}{\sqrt{2}}. \tag{18}$$

The EUSO-SPB1 energy limits are indicated in the bottom plots in Fig. 11 for EUSO-TA elevation angles of 10° and 25°. The energy limits of EUSO-SPB1 estimated in all combinations of background, elevation angle of EUSO-TA, and version of the electronics board (SPACIROC1 and SPACIROC3) are collected in Table 1 (from proton simulations) and Table 2 (from iron simulations), where the average energies over different elevation angles and for the same background and electronics board are shown in bold type. They are also drawn in the middle and bottom plots of Fig. 15, where they are superimposed on real EUSO-TA measurements and on the energy corresponding to the 100% EUSO-SPB1 trigger rate estimated in previous analysis with both measurements and simulations (see Section 4.3.1).

In general, there is no significant difference in the results from proton and iron simulations. For elevation angle 15° and background 1 count/pixel/GTU, the results differ from the trend set by the other

Table 1
Energy limit of EUSO-SPB1 estimated from EUSO-TA simulations (with proton primaries) in different conditions of background, elevation angle of EUSO-TA, version of the electronics board (SPACIROC1 and SPACIROC3), and considering both $D = a \cdot E + b$ ($D \propto E$) and $D = a \cdot \sqrt{E} + b$ ($D \propto \sqrt{E}$) as the limit function. In bold are the average energies over different elevation angles and for the same background and electronics board.

Proton					
Background	Elevation	$E^{\text{limit}}_{\text{EUSO-SPB1}}$ (eV)			
(c./p./GTU)	(deg)	SPACIROC1		SPACIROC3	
		$D \propto E$	$D \propto \sqrt{E}$	$D \propto E$	$D \propto \sqrt{E}$
1	10	1.50×10^{18}	1.81×10^{18}	1.55×10^{18}	1.76×10^{18}
1	15	3.52×10^{18}	6.88×10^{18}	2.82×10^{18}	4.31×10^{18}
1	20	1.55×10^{18}	1.40×10^{18}	1.58×10^{18}	1.71×10^{18}
1	25	1.99×10^{18}	1.60×10^{18}	1.60×10^{18}	1.84×10^{18}
Average energy limit		$\mathbf{2.14 \times 10^{18}}$	$\mathbf{3.17 \times 10^{18}}$	$\mathbf{1.89 \times 10^{18}}$	$\mathbf{2.41 \times 10^{18}}$
1.5	10	3.20×10^{18}	4.91×10^{18}	2.91×10^{18}	3.64×10^{18}
1.5	15	2.95×10^{18}	4.28×10^{18}	3.15×10^{18}	3.94×10^{18}
1.5	20	3.36×10^{18}	4.04×10^{18}	4.38×10^{18}	5.34×10^{18}
1.5	25	3.88×10^{19}	5.87×10^{18}	3.40×10^{18}	3.46×10^{18}
Average energy limit		$\mathbf{3.35 \times 10^{18}}$	$\mathbf{4.77 \times 10^{18}}$	$\mathbf{3.46 \times 10^{18}}$	$\mathbf{4.19 \times 10^{18}}$

Table 2
Energy limit of EUSO-SPB1 estimated from EUSO-TA simulations (with iron primaries) in different conditions of background, elevation angle of EUSO-TA, version of the electronics board (SPACIROC1 and SPACIROC3), and considering both $D = a \cdot E + b$ ($D \propto E$) and $D = a \cdot \sqrt{E} + b$ ($D \propto \sqrt{E}$) as the limit function. In bold are the average energies over different elevation angles and for the same background and electronics board.

Iron					
Background	Elevation	$E^{\text{limit}}_{\text{EUSO-SPB1}}$ (eV)			
(c./p./GTU)	(deg)	SPACIROC1		SPACIROC3	
		$D \propto E$	$D \propto \sqrt{E}$	$D \propto E$	$D \propto \sqrt{E}$
1	10	1.76×10^{18}	1.67×10^{18}	1.25×10^{18}	2.00×10^{18}
1	15	2.98×10^{18}	3.70×10^{18}	2.98×10^{18}	3.70×10^{18}
1	20	2.64×10^{18}	3.73×10^{18}	1.68×10^{18}	1.17×10^{18}
1	25	1.75×10^{18}	2.25×10^{18}	1.96×10^{18}	1.16×10^{18}
Average energy limit		$\mathbf{2.28 \times 10^{18}}$	$\mathbf{2.84 \times 10^{18}}$	$\mathbf{1.97 \times 10^{18}}$	$\mathbf{2.26 \times 10^{18}}$
1.5	10	2.55×10^{18}	2.63×10^{18}	2.33×10^{18}	3.51×10^{18}
1.5	15	2.91×10^{18}	2.99×10^{18}	3.96×10^{18}	4.62×10^{18}
1.5	20	4.15×10^{18}	4.22×10^{18}	3.23×10^{18}	3.78×10^{18}
1.5	25	5.14×10^{19}	5.77×10^{18}	2.46×10^{18}	2.57×10^{18}
Average energy limit		$\mathbf{3.69 \times 10^{18}}$	$\mathbf{3.90 \times 10^{18}}$	$\mathbf{2.99 \times 10^{18}}$	$\mathbf{3.62 \times 10^{18}}$

elevation angles. This is addressable only on statistical effects. The trend seems to be that for low background, SPACIROC3 allows reaching lower energy limits for EUSO-SPB1 than SPACIROC1, and vice versa for high background. In principle, SPACIROC3 should always perform better than SPACIROC1, as with its higher double-pulse resolution it can sample more photons in the same time frame. This makes it possible to detect more showers. Moreover, with SPACIROC3 some non-detected showers overcome the cut on the number of counts used in the analysis, while do not with SPACIROC1: in the first case they would be included in the analysis and in the latter would be excluded. The difference in the performance (with low and high background) is most likely due to both the statistics of the simulated events and the aforementioned effects. For example, in some cases with high background a few events at relatively low distance and energy resulted in triggers with SPACIROC3 but not with SPACIROC1. This has tilted the limit line resulting to be at lower energies for short distances and at higher energies for long distances, causing an increase in the energy limit of EUSO-SPB1. However, in the context of this analysis, the average values are taken into account to estimate a range of energy that, according to this approach, includes the detection limit of EUSO-SPB1.

The counts measured by the detector for each event can provide information to discriminate between triggered and non-triggered events, too. In Fig. 14 the total number of counts (excluding the background) with respect to $E_{\text{eq,atm}}$ (top) and the distance (bottom) of each triggered and non-triggered shower are shown, for elevation angles of 10° (left) and 25° (right). Lines represent the limit evaluated for counts versus energy and versus distance, following the procedure used to separate events in the distance versus energy frame. The functions used for the limit of counts (C) versus distance (D) are $C = a \cdot D + b$ ($c \propto D$) and $C = a/D^2 + b$ ($C \propto 1/D^2$), being valid the considerations made in the evaluation of the limit in the frame distance versus energy. For the limit of counts versus energy, a linear equation $C = a \cdot E + b$ is used. The values of the parameters are collected in Tables E.12 and E.10 for proton and Tables E.13 and E.11 for iron.

In these plots, one can see that the number of counts increases with the energy and decreases with the distance, as expected. For both elevation angles, the triggered showers generate at least ~200 counts. The minimum number of counts for the triggered showers tends to decrease as the distance increases. This is because increasing the distance of the showers, the FOV of single pixels increase and therefore the track at the focal surface becomes narrower than a MAPMT size. On the other hand, close showers have broad tracks with high-counts pixels distributed through most of the MAPMTs. In this way, far away showers might be triggered even with lower counts than close showers.

4.3. Analysis of the data

4.3.1. Detection limit via analysis of the measured data

The same procedure used to study the detection limit of EUSO-TA with simulations, described in Section 4.2.2, was applied also to the data. In this case, the original energy to be corrected (for the fact that only a portion of shower was observed and for the atmospheric transmission) is the energy reconstructed in monocular mode by the Telescope Array Collaboration using the TA-BRM-FDs. The distance provided by the reconstruction is the impact parameter. By considering their distance to EUSO-TA measured inside its FOV and by applying the correction to the energy of the showers, as discussed in Section 4.1, the results from simulations can be compared with those from data. Furthermore, the detection limits evaluated via simulations can be tested on the data.

In Fig. 15 showers that crossed the FOV of EUSO-TA are shown. Green stars represent the detected shower events and red crosses the non-detected ones.

In the top-left panel, showers are represented with E_{recTA} and their distance measured along the line of sight of the detector. Since the distance of the shower along the telescope axis is usually larger than (or at most equal to) the impact parameter, all the points move towards larger distances than in Fig. 3, where the detected and non-detected events are shown with their impact parameter and reconstructed energy. The typical uncertainty of the energy reconstructed in monocular mode by the Telescope Array Collaboration is, as already mentioned, 17% [20].

In the following plots of Fig. 15, the energy is corrected with conversion factors calculated through simulations of proton-generated showers. The corresponding plots for iron-generated showers are in Fig. B.19.

In the top-right panel, showers are plotted with their equivalent energy E_{eq} (calculated with conversion factors considering proton primaries) and the distance. As the equivalent energy of the shower is usually lower than (or at most equal to) the reconstructed energy, the points move to lower energies with respect to the former plot. The uncertainty of the equivalent energy is the root sum square of the uncertainty on the reconstructed energy and that on the energy conversion factor (the standard deviation of the mean of the conversion factors estimated for showers with the same characteristics and at the same distance from EUSO-TA).

Calculating the energy corrected for the atmospheric transmission $E_{\text{eq,atm}}$ results in the shower distributions shown in the middle and

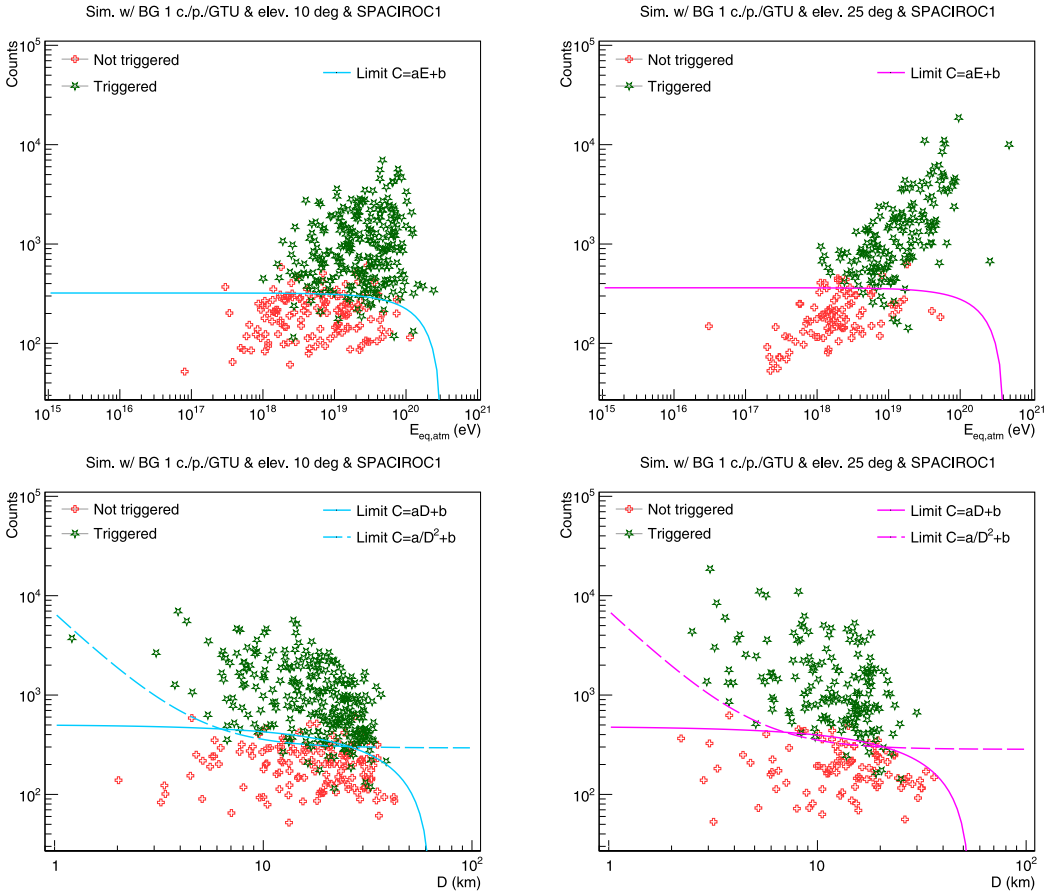

Fig. 14. Number of counts per event (excluding the background) with respect to its $E_{\mathrm{eq,atm}}$ (top) and distance (bottom), for triggered and non-triggered showers. Plots are for both 10° (left) and 25° (right) elevation angles. Lines represent the functions that separate triggered and non-triggered events.

bottom panels. The limits evaluated for the triggered and the non-triggered showers via simulations, for different elevation angles of EUSO-TA and considering both $D = a \cdot E + b$ and $D = a \cdot \sqrt{E} + b$ as trends of the EUSO-TA detection limit, are overlayed. Results are shown for both background levels 1 (middle panels) and 1.5 counts/pixel/GTU (bottom panels) and for SPACIROC1 (left) and SPACIROC3 (right) electronics boards. The uncertainty on the energy $E_{\mathrm{eq,atm}}$ is the same as for E_{eq}.

Statistics are naturally higher for showers at low energies with respect to high energies. In general, measured showers have reconstructed (by TA) energies in the range $1 \times 10^{17} - 6 \times 10^{18}$ eV. In simulations, a wide range of energy was considered ($1 \times 10^{17} - 1 \times 10^{20}$ eV), and the energy limits resulted to be in the range $1 \times 10^{18} - 1 \times 10^{19}$ eV, for the distances involved (up to about 20 km). Therefore, most of the showers in the data are at lower energies with respect to the detection limits from simulations, even the detected ones, as happens also in simulations for a minority of triggered showers. This is due to the fact that the EUSO-TA design is not optimized for ground-based observations (and therefore the energy limits are relatively high), while the TA experiment has a higher exposure to UHECRs.

The energy limits for EUSO-SPB1, calculated as the average of the energy limits for different elevation angles of EUSO-TA (the values in bold fonts in Tables 1 and 2), are overlayed separately for $D = a \cdot E + b$ and $D = a \cdot \sqrt{E} + b$, with a green full-circle and a pink full-cross, respectively. The horizontal bar for both markers covers the interval of possible values with different elevation angles between 10° and 25°.

To include a reference for EUSO-SPB1 from real measurements, results from the laser acquisitions made with EUSO-SPB1 at the EUSO-TA site before the launch were considered. EUSO-SPB1 operated with its own trigger algorithm, different from the EUSO-TA one. In [14] it is reported that a laser event with energy 0.8 mJ produces a similar number of counts to a simulated shower with energy 3×10^{18} eV observed from 33 km altitude. The energy of these events corresponds to 40% trigger efficiency. For reference purposes, this energy was rescaled in order to retrieve the 100% trigger rate, resulting to be $E^{100\%}_{EUSO-SPB1} = 5.63 \times 10^{18}$ eV and represented with an asterisk-like marker at a distance of 27 km, assumed as the distance of EUSO-SPB1 from the maximum of a sample shower (see Section 4.2.2). The energy limits for EUSO-SPB1 evaluated from simulations of EUSO-TA are lower than $E^{100\%}_{EUSO-SPB1}$, which makes the results from simulations consistent with those from measurements, also considering that the firsts have not been estimated with the trigger algorithm developed for EUSO-SPB1 but with that of EUSO-TA, and therefore the performance are lower.

In addition, in the middle and bottom plots, laser events from the CLF and the GLS (with two energies), are plotted with triangles and squares, respectively. As the laser events are clearly visible above the night sky background, their energies have to be much higher than the limits at the same distance, and indeed they are on the right side and far from the limit.

4.3.2. Analysis of the measured data via simulations

By means of the reconstruction parameters provided by the Telescope Array Collaboration, i.e. the energy, zenith, and azimuth angles, and the coordinates of the shower cores on ground, it was possible to simulate the showers that crossed the FOV of EUSO-TA and the detector response for each observation. The simulation of the showers was performed with the combination of CONEX and Offline simulations,

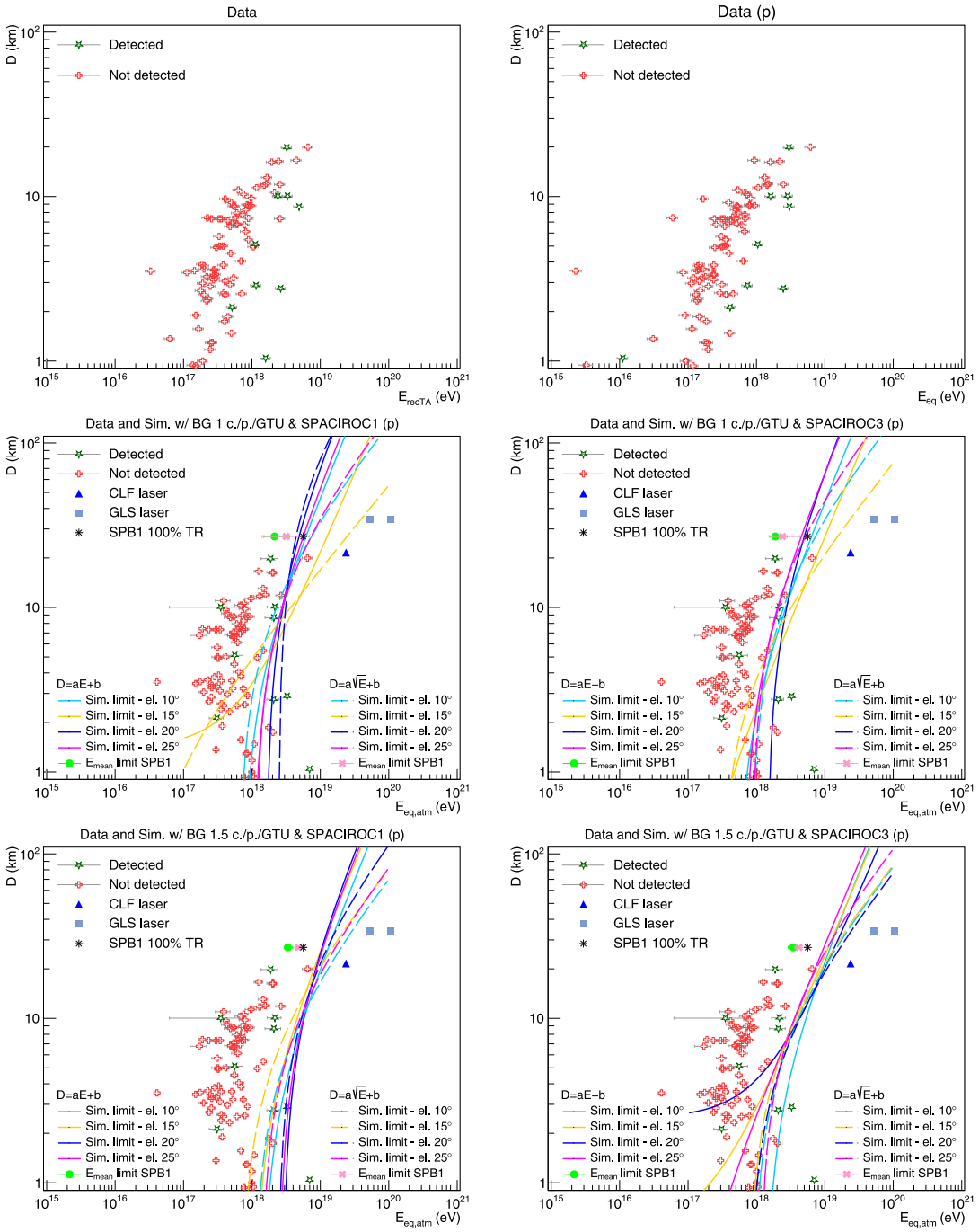

Fig. 15. Showers crossing the FOV of EUSO-TA during measurements displayed at different steps of the energy correction and with the detection limits from simulations overlapped (proton primaries). Distance of showers vs. the reconstructed energy (top-left); distance vs. equivalent energy (top-right); distance vs. equivalent energy corrected by the atmospheric attenuation (middle and bottom panels, where the positions of the shower events are the same). In the middle and bottom panels, the detection limits from simulations are overlapped, colors indicate different elevation angles and solid and dashed lines represent limits evaluated as $D = a \cdot E + b$ and $D = a \cdot \sqrt{E} + b$, respectively. In the middle plots, limits were estimated with the background level of 1 count/pixel/GTU, while in the bottom plots with the background of 1.5 counts/pixel/GTU; on the left are limits for SPACIROC1 boards and on the right for SPACIRCOC3 boards. In these plots, the energy thresholds for EUSO-SPB1 estimated from EUSO-TA simulations are indicated, as well as the energy at which EUSO-SPB1 performed 100% trigger rate (TR) during field tests.

in a similar way to what was discussed in Section 4.2.1. One proton shower was simulated per event, and the energies were rescaled using the conversion factors calculated via proton shower simulations.

In Fig. 16 the total number of counts from simulations are plotted with respect to $E_{\mathrm{eq,atm}}$ (left) and the distance (right). Only showers with $E_{\mathrm{recTA}} > 2.51 \times 10^{17}$ eV were simulated and are present in these plots, as at lower energies there were no detected events and therefore no more information to distinguish between detected and non-detected events could be obtained. The total number of counts is the sum of the counts per GTU in each event and excludes the background.

Both plots indicate that, in general, the simulated showers reproducing the detected events produce a higher number of counts with respect to those reproducing the non-detected events, with an average minimum value of ~300 counts. As discussed for simulations, the minimum number of counts for the detected showers tends to decrease as the distance increases.

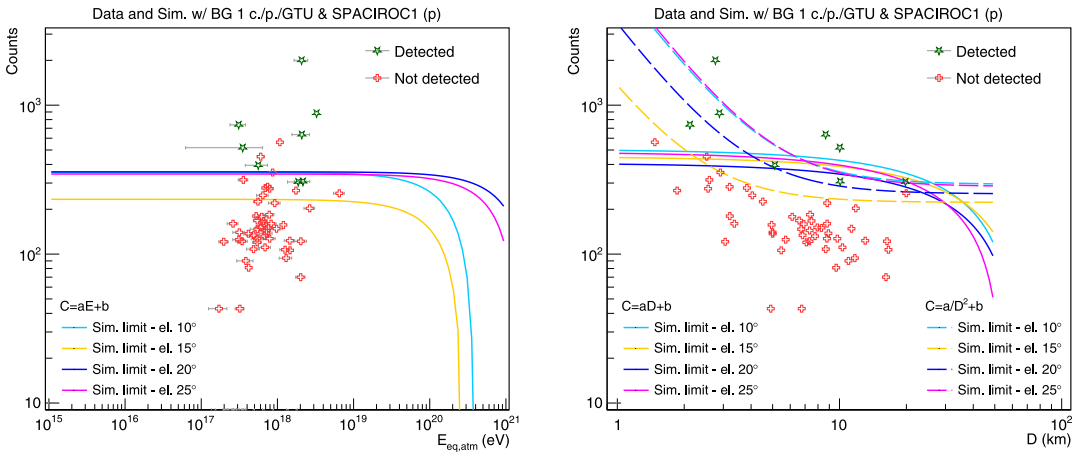

Fig. 16. Counts obtained from the simulation of the detected and non-detected events, with respect to $E_{\mathrm{eq,atm}}$ (left) and the distance (right). One detected event is missing because it was not possible to simulate it due to a technical issue possibly related to its short distance to the detector. Only showers with $E_{\mathrm{recTA}} > 2.51 \times 10^{17}$ eV were simulated and are present in these plots.

As done for plots in Fig. 15, the data points are overlapped by lines representing the detection limits in terms of counts as a function of the energy and the distance, evaluated from simulations (see Section 4.2.2). The parameters of the equations are collected in Tables E.10 and E.11. In general, the detected events tend to have number of counts above the threshold indicated by the limits from simulations.

4.4. Study of the level-1 trigger rates via simulations

The foreseen upgrade of EUSO-TA includes the self-trigger capability, to operate independently from the TA-BRM-FDs. For this purpose, dedicated trigger logics are needed. The level-1 trigger logic that operates on the 2.5 μs timescale for the observation of showers, was designed and implemented in the Offline framework, in order to test it through simulations and evaluate the UHECRs trigger rate.

The sets of simulations discussed in Section 4.2.1 were used also in this analysis, considering both proton and iron as primary cosmic ray. As the spectral index used in the simulations was −1, the energy distributions must be rescaled based on measured fluxes of UHECRs, to estimate the EUSO-TA trigger rate. For this purpose, both the energy fluxes measured with the Telescope Array (TA) experiment [32] and the Pierre Auger Observatory (PAO) [33] were used. The flux measured by the TA included showers with energy $E > 10^{17.2}$ eV and zenith angle $\theta < 65°$, while that measured by the PAO included showers with zenith angle $\theta < 40°$.

In Fig. 17 the energy distributions of showers generated by protons are presented, while those for iron showers are in Fig. B.20. In the top plots, the energy distributions of the simulated showers with spectral index −1 are shown.

The plots are for both the elevation angles 10° (left) and 25° (right) and for SPACIROC1 ASIC board. Black lines represent the simulated showers, blue lines the showers in the FOV of EUSO-TA, and red lines the triggered showers. Solid lines are for all showers with no cuts; dashed lines show the distributions with cuts on the energy and the zenith angle corresponding to those used to measure the energy spectrum with the TA; the dotted lines show the distributions with a cut on the zenith angle corresponding to that used to measure the energy spectrum with the PAO. It is visible that showers start to be triggered at energies $\simeq 10^{18}$ eV, although a few events with lower energy were triggered too.

In the first step of the trigger rate calculation, the energy distributions of the simulated and the triggered events with the same cuts on the energy and/or the zenith angle used in the spectra measured by the TA and the PAO were rescaled. Also the distributions of the events in the FOV of EUSO-TA were rescaled, although this was not necessary for the analysis. Hereafter, equations refer to the triggered events, as they are of interest in this analysis, but the same is valid also to rescale the energy distributions of the simulated events and of those in the FOV. For each i-th bin, we calculate the number of expected triggered events $n^{\mathrm{cut}}_{\mathrm{trig,exp,i}}$ with the limits applied by the quality cuts and in the time interval of $t_{123\,\mathrm{h}} = 123$ h, which is the active observation time during the data acquisitions in 2015 used as a reference:

$$n^{\mathrm{cut}}_{\mathrm{trig,exp,i}}\,(t_{123\,\mathrm{h}}) = \frac{n^{\mathrm{cut}}_{\mathrm{trig,i}}}{n^{\mathrm{cut}}_{\mathrm{sim,i}}} \cdot S^{\mathrm{cut}}_{\mathrm{EUSO-TA}} \cdot F^{\mathrm{cut}}_{\mathrm{i}} \cdot \mathrm{d}E_{\mathrm{i}} \tag{19}$$

where $n^{\mathrm{cut}}_{\mathrm{trig,i}}$ and $n^{\mathrm{cut}}_{\mathrm{sim,i}}$ are the number of triggered and simulated events, respectively; $S^{\mathrm{cut}}_{\mathrm{EUSO-TA}} = A \cdot \Omega \cdot t_{123\,\mathrm{h}}$ is the exposure of EUSO-TA, with $A = 36{\times}28$ km^2 $= 1008$ km^2 the area where showers were simulated and $\Omega = \pi \cdot \sin^2\theta_{\mathrm{max}}$ the solid angle corresponding to the maximum zenith angle considered ($\theta_{\mathrm{max}} = 65°$ for the flux from the TA and $\theta_{\mathrm{max}} = 40°$ for that from the PAO); $F^{\mathrm{cut}}_{\mathrm{i}}$ is the flux measured with the PAO or the TA; $\mathrm{d}E_{\mathrm{i}} = \ln(10) \cdot \bar{E}_{\mathrm{i}} \cdot 0.1 \simeq E_{\mathrm{max,i}} - E_{\mathrm{min,i}}$ is the differential energy, $\bar{E}_{\mathrm{i}}$ being the average energy and $E_{\mathrm{max,i}}$ and $E_{\mathrm{min,i}}$ the maximum and minimum energy, respectively. The rescaled distributions are visible in the bottom panels of Fig. 17, in black for the simulated events, in blue for those in the FOV of EUSO-TA, and in red for the triggered ones; dashed lines correspond to the quality cuts applied in the TA spectrum and dotted lines to that applied in the PAO spectrum.

In the second step, the limits imposed by the quality cuts were removed. The number of expected triggered events in the i-th bin $n_{\mathrm{trig,exp,i}}$ with no cuts was estimated by rescaling the number of triggered events with cuts in the same bin $n^{\mathrm{cut}}_{\mathrm{trig,exp,i}}$ (already corrected by the measured flux) with the ratio between the total number of events N_{trig} and the total number of events with cuts $N^{\mathrm{cut}}_{\mathrm{trig}}$, as follows:

$$n_{\mathrm{trig,exp,i}}\,(t_{123\,\mathrm{h}}) = \frac{N_{\mathrm{trig}}}{N^{\mathrm{cut}}_{\mathrm{trig}}} \cdot n^{\mathrm{cut}}_{\mathrm{trig,exp,i}}\,(t_{123\,\mathrm{h}}). \tag{20}$$

The corresponding distributions are plotted in the bottom plots of Fig. 17 with magenta and green dashed lines, considering the TA and the PAO spectrum, respectively. The cut on the zenith angle used for the PAO spectrum ($\theta < 40°$) was considerably reducing the statistics of simulated events, as can be seen in the distribution of triggered events with this cut in Fig. 17, where some bins are empty. This would have affected the rescaled distributions and ultimately the trigger rate. As the flux per bin measured by the PAO with $\theta < 40°$ differs only by a few percent from that measured with the same experiment with $\theta <$

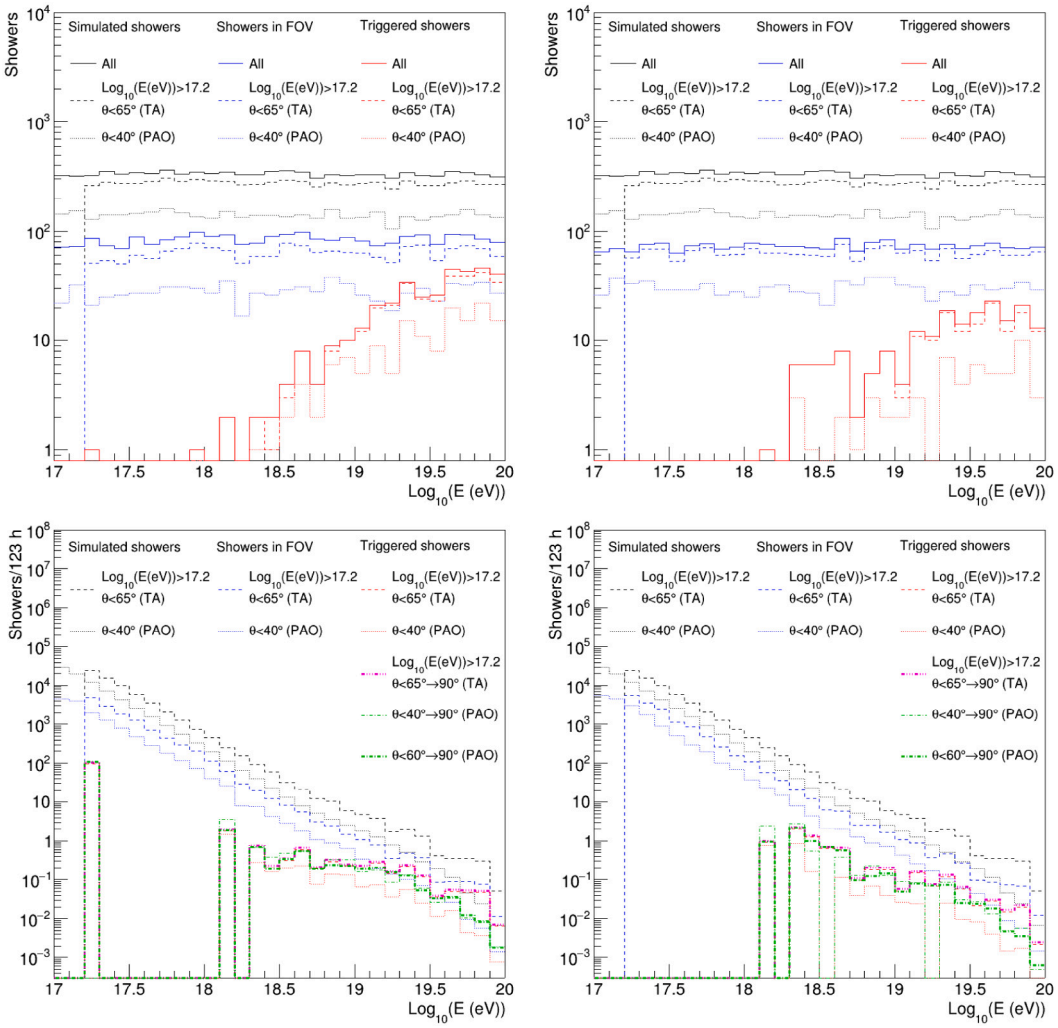

Fig. 17. Energy distribution of the simulated showers with proton primaries, spectral index −1 (top) and rescaled by the UHECR flux measured by the PAO and the TA, to retrieve the realistic ones (bottom). Plots are for elevation angles 10° (left) and 25° (right) and for SPACIROC1 ASIC boards. Black lines represent all the simulated showers, blue lines showers in the FOV of EUSO-TA, and red lines the triggered showers. Solid lines are for all showers with no cuts. The dashed and dotted lines show the distributions with cuts on the energy and zenith angle used to measure the energy spectrum with the TA and the PAO, respectively. In the rescaled distributions (bottom), the triggered showers are split considering the TA and the PAO spectrum, plotted with magenta and green dashed lines, respectively.

60° [34],[2] the flux with $\theta < 40°$ was applied to a larger set of simulated events with $\theta < 60°$. The results obtained by this procedure are more stable. Therefore, the final distributions of triggered events rescaled using the fluxes by the TA and the PAO are presented in bottom plots of Fig. 17 with thick lines, in magenta and green, respectively.

The potential trigger rate per bin in 123 h, T_R (123 h), was calculated as the sum of the expected events per bin (i.e. the integral of the energy distribution):

$$T_R\,(t_{123\,h}) = \sum_{i=10}^{N_{bins}} n_{trig,exp,i}\,(t_{123\,h}). \tag{21}$$

A few simulated events with energy $E < 10^{18}$ eV were triggered in special conditions, for example with a strong component of Cherenkov photons contributing to the overall signal (which happens when the shower direction points towards the telescope), or events with very low counts, barely passing the trigger conditions. For these reasons, a few bins in the distributions in the plots at the top of Fig. 17 were populated by single events. After the rescaling for the UHECR flux, the same bins would contain tens to hundreds of expected triggered events as in the bottom-left plot in Fig. 17, introducing statistical artifacts in the results. To prevent outliers from affecting the trigger rate, only events with $E \geq 10^{18}$ eV (i.e. bin i ≥ 10, with i = 0 the first bin) were considered.

In Table 3 (proton) and Table 4 (iron) the trigger rates for different background levels and elevation angles of EUSO-TA are reported, considering both the SPACIROC1 and SPACIROC3 ASIC boards and both the PAO and TA measured flux to rescale the energy distributions. The rates correspond to the duration of the four observation sessions made in 2015 (123 h).

Thinking in terms of single acquisition sessions (of about 30 h each), these results indicate that, with the level-1 trigger, it could be possible to detect on average 1−2 showers/session in case of 1 count/pixel/GTU background level and SPACIROC1 boards. Using SPACIROC3 boards the trigger rates increase by 15−20%. With a higher background level of 1.5 counts/pixel/GTU, the trigger rates decrease with respect to those with a lower background level: this happens in a stronger way for SPACIROC1 than SPACIROC3, because with the latter the telescope is more sensitive and thus able to detect more showers.

In iron simulations, the average trigger rates are slightly lower than in the proton ones. However, in the case of iron, they increase regularly with the elevation angle of EUSO-TA, moreso than with protons. This

[2] The flux in [34] was limited to energies $E > 10^{18.4}$ eV, and to simplify the procedure and avoid problems of normalization between two sets of low- and high-energy spectra, the flux in [33] was considered in this study.

Table 3
Trigger rates for different background levels and elevation angles of EUSO-TA, considering both the SPACIROC1 and SPACIROC3 boards. Results are for proton primary cosmic rays.

Proton					
Background	Elevation	T_R (events/123 h)			
(c./p./GTU)	(deg)	SPACIROC1		SPACIROC3	
		Auger	TA	Auger	TA
1	10	5.2	6.1	5.5	6.4
1	15	7.3	9.4	7.7	10.0
1	20	6.0	6.9	7.6	8.7
1	25	6.2	7.1	8.3	9.5
Average trigger rate		**6.2**	**7.4**	**7.3**	**8.7**
1.5	10	2.0	2.6	2.5	3.3
1.5	15	1.9	2.4	3.6	4.3
1.5	20	3.0	3.4	4.9	5.5
1.5	25	3.2	3.5	8.3	8.7
Average trigger rate		**2.5**	**3.0**	**4.8**	**5.5**

Table 4
Trigger rates for different background levels and elevation angles of EUSO-TA, considering both the SPACIROC1 and SPACIROC3 boards. Results are for iron primary cosmic rays.

Iron					
Background	Elevation	T_R (events/123 h)			
(c./p./GTU)	(deg)	SPACIROC1		SPACIROC3	
		Auger	TA	Auger	TA
1	10	3.3	4.1	4.0	5.0
1	15	4.0	5.0	6.6	7.9
1	20	6.3	7.6	7.6	10.0
1	25	7.8	8.6	9.7	10.6
Average trigger rate		**5.3**	**6.3**	**7.0**	**8.4**
1.5	10	0.8	1.1	1.4	1.9
1.5	15	1.2	1.6	3.6	4.2
1.5	20	3.5	3.8	4.4	5.3
1.5	25	4.4	5.3	5.7	6.8
Average trigger rate		**2.5**	**2.9**	**3.8**	**4.4**

can be explained by the fact that the distribution of the X_{max} in iron showers is at lower values (higher in the atmosphere) and narrower than in the proton ones [35], and therefore showers with the same energy and direction have similar longitudinal profiles.

For reference, four showers were triggered by applying offline, i.e. on the already acquired data, the level-1 trigger algorithm on the data collected with the external trigger in 2015, during which the EUSO-TA operated with the SPACIROC1 board and the background level changed (depending on the sky condition, day, and time of the acquisition). In this way, we estimated a rate of about 1 shower/session.

Therefore, the rates estimated from simulations, with SPACIROC1 boards, of 1−2 showers/session with low background and 0.5−1 showers/session with higher background are consistent with the rate estimated by applying the level-1 trigger on the collected data of 1 shower/session. Only by processing the data with several methods, a total of nine showers were identified, or about 2 showers/session.

5. Summary and conclusion

EUSO-TA demonstrates the performance of a new detector technology for the observation of UHECRs, based on an optical system made of Fresnel lenses and a focal surface composed of a matrix of MAPMTs. The detector system was designed for observations from space within the JEM-EUSO program but performs well also on the ground. The detector registered, using the TA-BRM-FD external trigger, nine UHECRs events during its four acquisition sessions in 2015. The response of the detector was also tested using UV laser shots mimicking extensive air showers. An optimization of the detector will be achieved through hardware and firmware upgrades. This will allow remote operations of EUSO-TA and will provide detector self-triggering, so that the instrument can operate independently of the TA-BRM-FDs.

In order to evaluate the detection limit of EUSO-TA as a function of the shower energy and distance from the detector, a method was developed to rescale the real energy taking into account that only a portion of the shower can be observed by the detector. Such a method was then applied to several sets of simulations. The showers were simulated with proton and iron primaries, different energies ($1 \times 10^{17}-1 \times 10^{20}$ eV) and directions (zenith angle in the range 0°−90° and azimuth angle in the range 0°−360°), and distributed on the EUSO-TA site, in order to reproduce several realistic conditions. EUSO-TA was simulated with the self-trigger capability and with two electronics configurations: the one used at the time of the measurements performed in 2015 (SPACIROC1 board), and that foreseen for the upgraded EUSO-TA2 (SPACIROC3 board). Two background levels were considered (1 and 1.5 counts/pixel/GTU). For all configurations, the detection limit was evaluated. The overall results are that the energy limit is in the range $1 \times 10^{18}-1 \times 10^{19}$ eV in the range of distances involved (up to 50 km), although, occasionally, showers can be detected also at lower energies.

The detection limits estimated from simulations (with the EUSO-TA internal trigger) were compared to the real data (acquired with the external trigger from TA-BRM-FDs). Due to the natural higher statistics of showers at the (relatively) low energies, the EUSO-TA design optimized for space-based observations, and the higher TA exposure to UHECRs observed from the ground, most of the showers that crossed the FOV of EUSO-TA during real measurements are at lower energies than the energy limit from simulations.

The sensitivity of EUSO-TA can be extended also to the EUSO-SPB1 balloon-based experiment, which is similar to EUSO-TA in design and for which the distance of observation (33 km altitude, or lower when considering the observation of the shower maximum at a few km from the ground) is of the order of the longest distances from which EUSO-TA can detect showers. The energy limit estimated for EUSO-SPB1 is in the range $2-5\times10^{18}$ eV, consistent with the energy at which EUSO-SPB1 performed 100% trigger rate during field tests at the EUSO-TA site that is, as expected, higher than the energy limits. There is no significant difference in the results from proton and iron simulations.

An analysis of the internal trigger performance was also done, using the aforementioned simulation sets for both proton and iron showers. The expected trigger rate is of about 1−2 detections per acquisition session (of about 30 h each), in the case of low background level (1 count/pixel/GTU) and SPACIRCOC1 boards. By using SPACIROC3 boards, the trigger rates increase 15%−20%. For the higher background level (1.5 counts/pixel/GTU) the rates halve. Running the level-1 trigger algorithm on the real data (measured when the detector hosted SPACIROC1 electronic boards), it was possible to detect about one shower per acquisition session. Considering that the background level changed depending on the sky condition and time of the acquisition, the results of the simulations are consistent with that rate. The average trigger rates of iron showers are slightly lower than those for protons, but they increase more regularly with the elevation angle of EUSO-TA than proton showers. This is due to the fact that the X_{max} distribution for iron showers is at lower values (higher in the atmosphere) and narrower than for the proton ones, reducing the difference between showers with the same characteristics.

CRediT authorship contribution statement

J.H. Adams Jr.: Conceptualization. **L. Anchordoqui:** Conceptualization. **D. Barghini:** Conceptualization. **M. Battisti:** Methodology, Formal analysis, Data curation, Conceptualization. **A.A. Belov:** Resources, Conceptualization. **J.W. Belz:** Conceptualization. **M. Bertaina:**

Writing – review & editing, Supervision, Methodology, Conceptualization. **F. Bisconti:** Writing – original draft, Software, Methodology, Formal analysis, Data curation, Conceptualization. **C. Blaksley:** Conceptualization. **S. Blin-Bondil:** Resources, Conceptualization. **F. Capel:** Data curation, Conceptualization. **M. Casolino:** Project administration, Investigation, Funding acquisition, Data curation, Conceptualization. **A. Cummings:** Conceptualization. **T. Ebisuzaki:** Data curation, Conceptualization. **J. Eser:** Software. **S. Falk:** Software. **F. Fenu:** Conceptualization. **S. Ferrarese:** Conceptualization. **G. Filippatos:** Software. **M. Fouka:** Software, Conceptualization. **C. Fuglesang:** Conceptualization. **P. Gorodetzky:** Conceptualization. **F. Guarino:** Software. **A. Haungs:** Writing – review & editing, Supervision, Conceptualization. **N. Inoue:** Conceptualization. **F. Kajino:** Conceptualization. **P.A. Klimov:** Conceptualization. **M. Manfrin:** Conceptualization. **L. Marcelli:** Conceptualization. **W. Marszał:** Software. **H. Mashiyama:** Software. **J.N. Matthews:** Resources, Conceptualization. **H. Miyamoto:** Conceptualization. **S. Ogio:** Conceptualization. **H. Ohmori:** Resources, Conceptualization. **A.V. Olinto:** Conceptualization. **E. Parizot:** Methodology, Conceptualization. **T. Paul:** Writing – review & editing, Software. **P. Picozza:** Conceptualization. **L.W. Piotrowski:** Writing – review & editing, Validation, Data curation. **Z. Plebaniak:** Writing – review & editing. **G. Prévôt:** Resources. **M. Przybylak:** Conceptualization. **E. Reali:** Resources. **M. Ricci:** Resources, Conceptualization. **H. Sagawa:** Writing – review & editing, Resources, Conceptualization. **Z. Sahnoun:** Software. **N. Sakaki:** Software. **H. Shin:** Resources, Investigation, Data curation. **K. Shinozaki:** Methodology, Conceptualization. **P. Sokolsky:** Resources. **J. Szabelski:** Resources, Conceptualization. **N. Tajima:** Resources. **Y. Takizawa:** Resources. **Y. Tameda:** Resources. **G.B. Thomson:** Resources. **M. Vrabel:** Resources, Data curation. **L. Wiencke:** Resources, Conceptualization. **M.Yu. Zotov:** Conceptualization.

Declaration of competing interest

The authors declare that they have no known competing financial interests or personal relationships that could have appeared to influence the work reported in this paper.

Data availability

Data will be made available on request.

Acknowledgments

The authors acknowledge all members of the JEM-EUSO Collaboration.

We are grateful to the Telescope Array Collaboration for allowing us to use the TA site and its facilities, and for all their help.

This work was supported by the Italian Ministry of Foreign Affairs and International Cooperation, by the Italian Space Agency through the ASI-INFN agreement n. 2020-26-HH.0, and n. 2021-8-HH.0 and its amendments, by the Deutsches Zentrum für Luft- und Raumfahrt, Germany, by the Helmholtz Alliance for Astroparticle Physics funded by the Initiative and Networking Fund of the Helmholtz Association (Germany), by the French space agency CNES, by National Science Centre in Poland grant n. 2020/37/B/ST9/01821, by the Interdisciplinary Scientific and Educational School of Moscow University "Fundamental and Applied Space Research". L. W. Piotrowski acknowledges financing by the Polish National Agency for Academic Exchange within Polish Returns Programme n. PPN/PPO/2020/1/00024/U/00001 and National Science Centre in Poland grant n. 2022/45/B/ST2/02889.

Appendix A. Parameters of the detected events from measurements with the external trigger from TA-BRM-FDs

This table collects the parameters of the nine events detected by EUSO-TA while it was operating, with different elevation angles, using the external trigger of TA-BRM-FDs. The elevation angle is in the first column; in the following four columns there are the parameters from the TA reconstruction; in the last two columns parameters calculated in this analysis (see Table A.5).

Table A.5
Parameters of the nine detected events from measurements with the external trigger from TA-BRM-FDs. In order from left to right: elevation angle of EUSO-TA during the operation; energy reconstructed by TA, zenith angle θ; azimuth angle ϕ measured from east counterclockwise; the impact parameter R_p; the energy rescaled based on this analysis $E_{eq,atm}$; the distance of the shower measured along the telescope optical axis.

elev. (deg)	E_{recTA} (eV)	θ (deg)	ϕ (deg)	R_p (km)	$E_{eq,atm}$ (eV)	D (km)
25	4.90×10^{18}	56.9	15.7	8.3	2.09×10^{18}	8.66
15	1.15×10^{18}	34.5	82.8	2.5	3.27×10^{18}	2.88
25	1.58×10^{18}	62.9	27.0	0.8	6.98×10^{18}	1.04
21	1.12×10^{18}	29.5	254.9	5.0	5.61×10^{17}	5.12
20	3.24×10^{18}	60.4	169.3	9.1	1.88×10^{18}	19.80
10	2.40×10^{18}	41.2	114.8	6.7	3.51×10^{17}	10.03
15	3.31×10^{18}	40.6	210.5	9.0	2.17×10^{18}	10.07
10	5.13×10^{17}	10.6	130.5	1.7	3.10×10^{17}	2.12
15	2.63×10^{18}	8.1	8.0	2.6	2.08×10^{18}	2.76

Appendix B. Plots from the analysis of iron showers

This appendix contains plots for iron primaries that are counterparts of those in the main body of the paper made for proton primaries.

B.1. Conversion factors with iron as primary cosmic ray

See Fig. B.18.

B.2. Data rescaled in energy with conversion factors from iron simulations

See Fig. B.19.

B.3. Event rate with iron primaries

Event rate of showers generated by iron primaries. For the description of the plots, refer to Section 4.4.

Appendix C. Shower core positions

In Fig. C.21, the shower core positions are plotted in the North/East frame in the Universal Transverse Mercator (UTM) system. The maps also show the position of EUSO-TA and the CLF, which are about 21 km apart. In the map on the top-left, the shower cores of all the simulated showers are drawn with gray squares, overlayed by those that entered the FOV drawn with blue squares, and those that were triggered drawn with red stars. In the other plots, showers are split according to their energy, zenith, and azimuth angles. Depending on the relative position between EUSO-TA and these shower cores, they are distributed over a different portion of the plots. In the map at the top-right, showers are split depending on the energy. Having simulated showers with an energy spectral index -1, most of the triggered showers have energy above 1×10^{19} eV and can reach distances of several tens of kilometers from EUSO-TA. At lower energies, the distance of the triggered showers gets smaller. In the map at the bottom-left, showers are split by the zenith angle. It is visible that showers with low zenith angles have the cores close to the optical axis of EUSO-TA, as it should be in order to have the shower in the FOV; by increasing the zenith angle, the position of the shower core gets farther from the optical axis. In the map at the bottom-right, showers are split by the azimuth angle. For reference, the azimuth angle 0° points towards the East (right) and increases counterclockwise. Also in this case, due to geometrical constraints, the shower cores are in different areas depending on the azimuth angle.

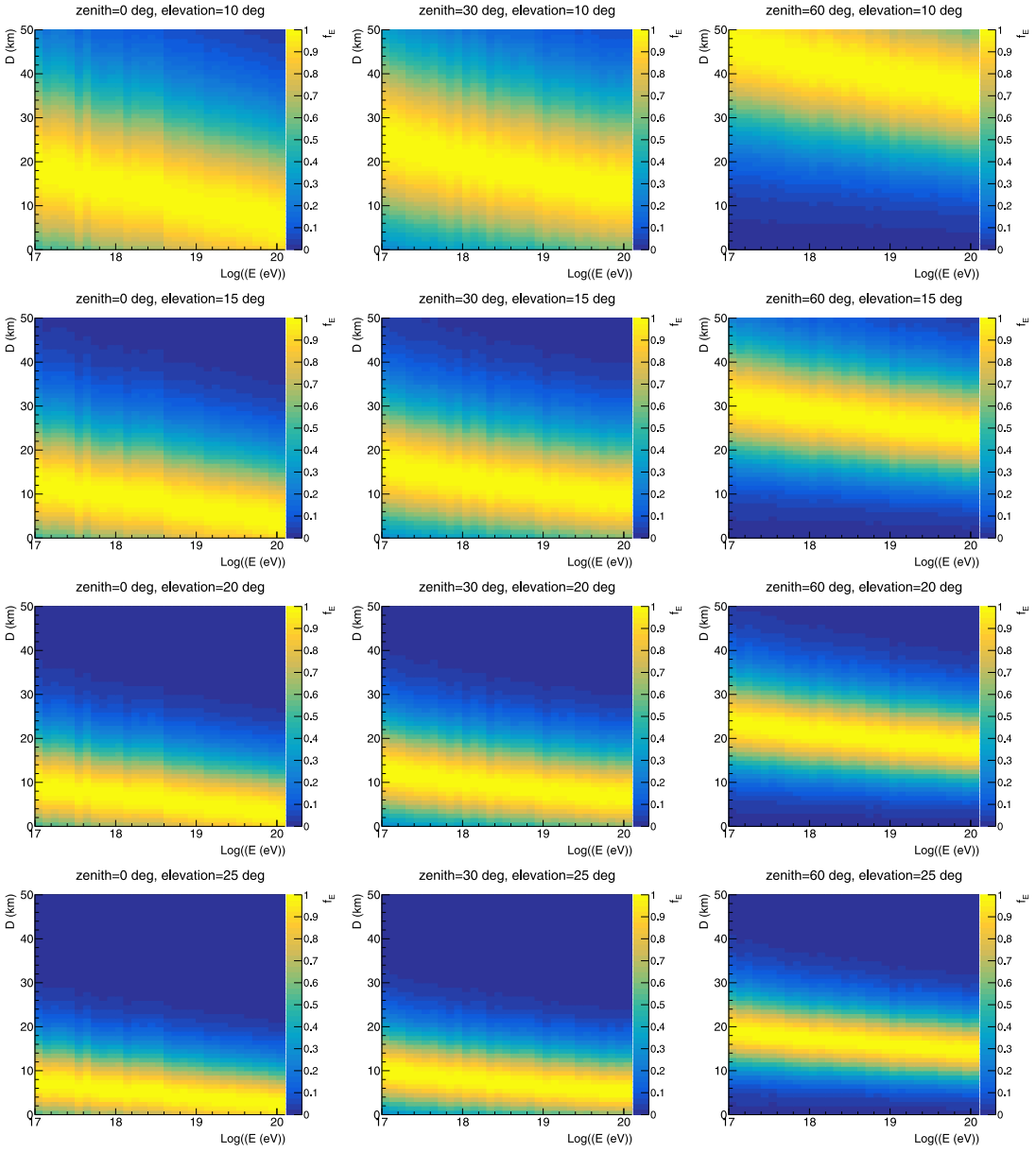

Fig. B.18. Energy conversion factors for iron primaries as a function of the shower energy and distance from the detector. The plots refer to 10°, 15°, 20°, and 25° elevation angles and 0°, 30°, and 60° zenith angles.

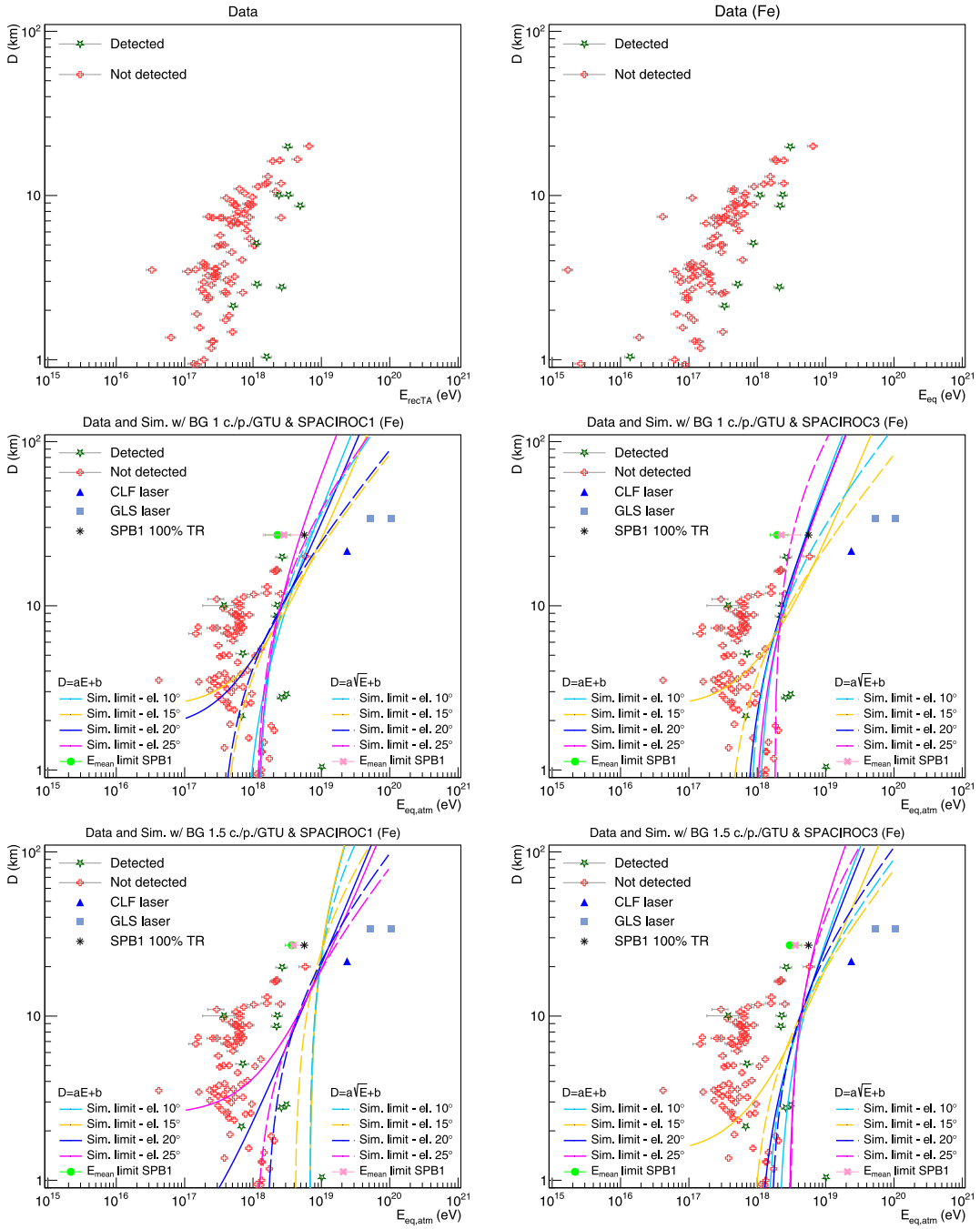

Fig. B.19. Showers crossing the FOV of EUSO-TA during measurements displayed at different steps of the energy correction and with the detection limits from simulations overlapped (iron primaries). Distance of showers vs. the reconstructed energy (top-left); distance vs. equivalent energy (top-right); distance vs. equivalent energy corrected by the atmospheric attenuation (middle and bottom panels, where the positions of the shower events are the same). In the middle and bottom panels, the detection limits from simulations are overlapped, colors indicate different elevation angles and solid and dashed lines represent limits evaluated as $D = a \cdot E + b$ and $D = a \cdot \sqrt{E} + b$, respectively. In the middle plots, limits were estimated with the background level of 1 count/pixel/GTU, while in the bottom plots with the background of 1.5 counts/pixel/GTU; on the left are limits for SPACIROC1 boards and on the right for SPACIRCOC3 boards. In these plots, the energy thresholds for EUSO-SPB1 estimated from EUSO-TA simulations are indicated, as well as the energy at which EUSO-SPB1 performed 100% trigger rate (TR) during field tests.

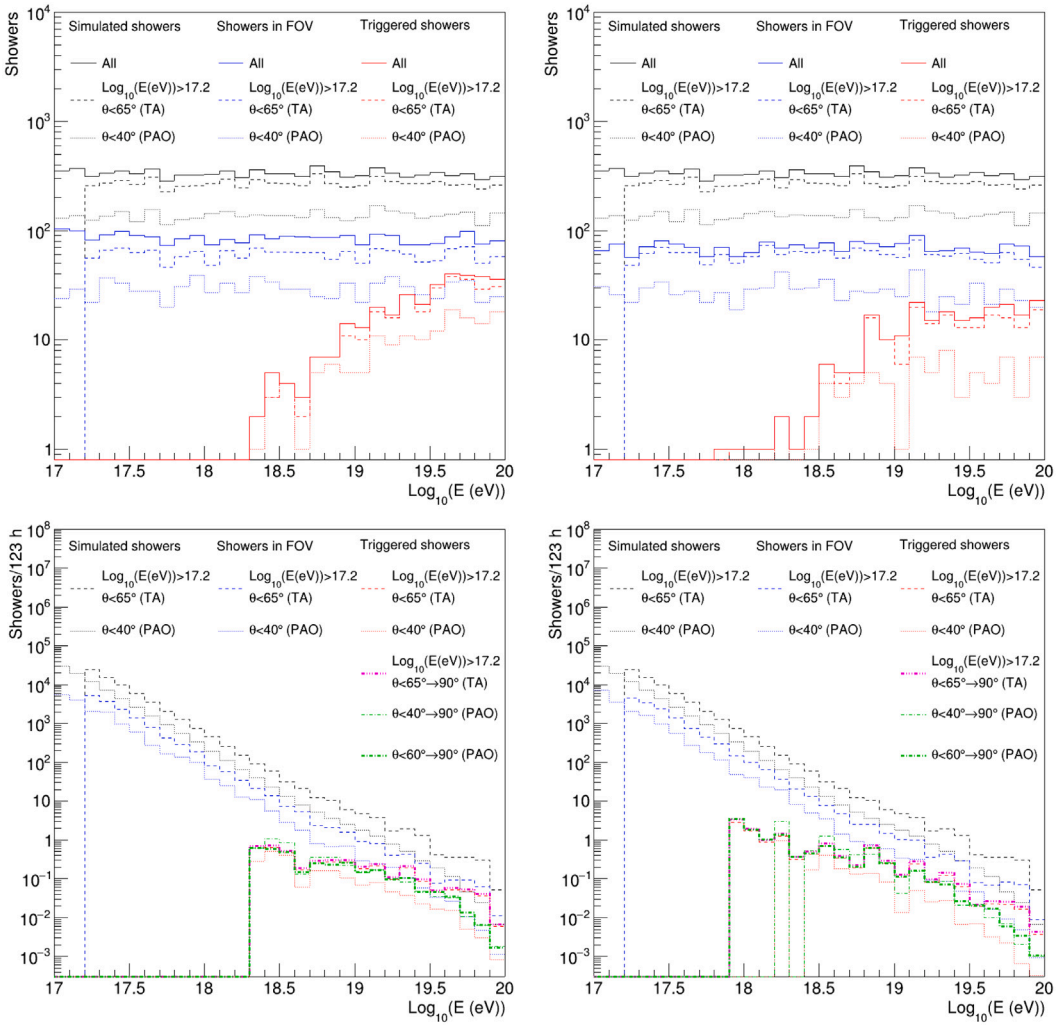

Fig. B.20. Energy distribution of the simulated showers with iron primaries, spectral index −1 (top) and rescaled by the UHECR flux measured by the PAO and the TA, to retrieve the realistic ones (bottom). Plots are for elevation angles 10° (left) and 25° (right) and for SPACIROC1 ASIC boards. Black lines represent all the simulated showers, blue lines showers in the FOV of EUSO-TA, and red lines the triggered showers. Solid lines are for all showers with no cuts. The dashed and dotted lines show the distributions with cuts on the energy and zenith angle used to measure the energy spectrum with the TA and the PAO, respectively. In the rescaled distributions (bottom), the triggered showers are split considering the TA and the PAO spectrum, plotted with magenta and green dashed lines, respectively.

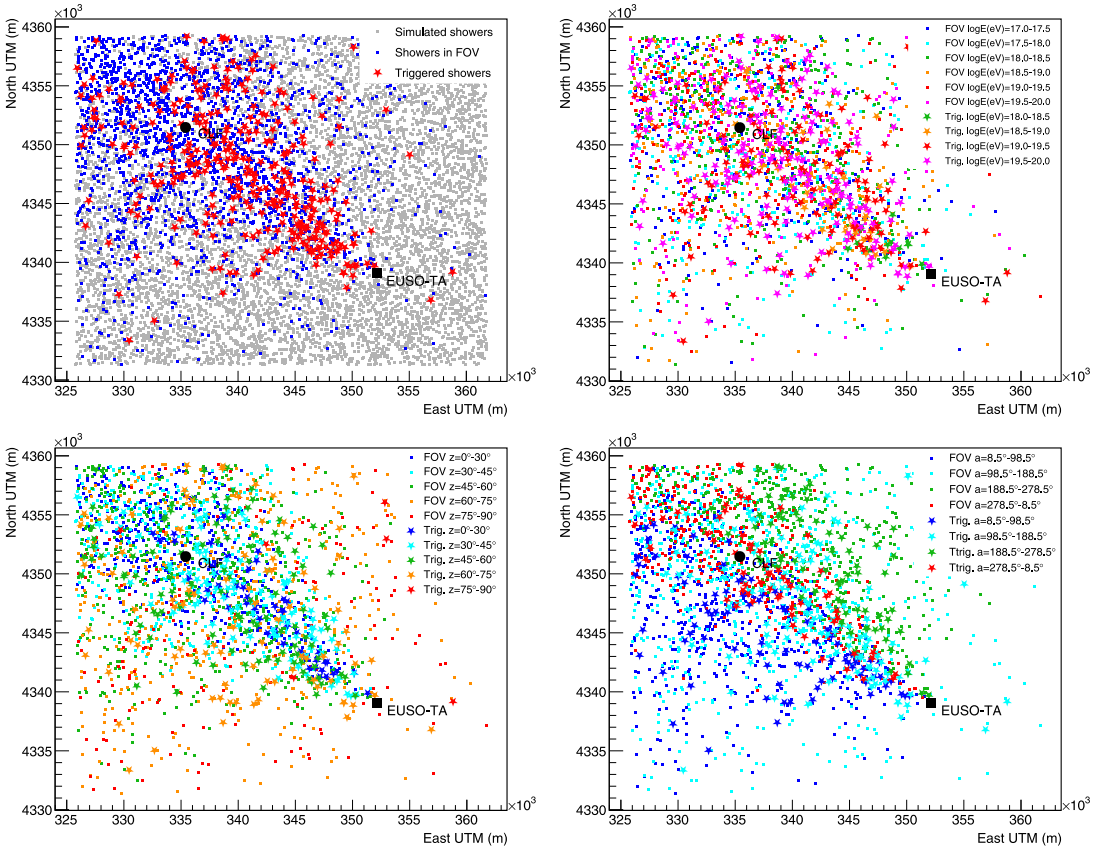

Fig. C.21. Position of the simulated shower cores plotted in the North/East frame in the UTM system. In the top-left plot, all shower cores are overlayed by those of showers that entered the FOV and those of the triggered ones. In the other maps, showers in the FOV and the triggered ones are split depending on the energy (top-right), the zenith (bottom-left) and the azimuth (bottom-right) angles.

Appendix D. Simulations of vertical showers

To exclude effects introduced by the random geometry of the simulated showers, a set of simulations was performed with vertical (proton) showers. This set of simulations is intended only to prove that with vertical showers a cleaner separation between the triggered and the non-triggered events can be reached. Indeed, using random directions some events could be triggered as a consequence of the Cherenkov emission of photons, but this contribution to the signal is not taken into account in the energy re-scaling. Moreover, random directions might produce some showers that cross the FOV of EUSO-TA only in the corners, generating too little signal to trigger. With vertical showers, these situations are largely avoided.

In Fig. D.22, the simulated vertical showers are plotted with their distance and simulated energy (top), equivalent energy (middle), and equivalent energy corrected for the atmospheric transmission (bottom). Plots are for background level of 1 count/pixel/GTU, elevation angle of 10° (left) and 25° (right), and SPACIROC1 electronics board. The same quality cuts listed in Section 4.2.2 have been applied to the showers, and the same procedures to draw the detection limit and to calculate the energy limit for EUSO-SPB1 were used. It is visible that there is almost no region where the triggered and the non-triggered events overlap. Only a few non-triggered events are in the region of the triggered ones, for cases in which the photons arrived on the focal surface of the instrument mainly in the gaps between MAPMTs, and therefore they were not recorded. At distances beyond 20 km, the non-triggered events overlap more the triggered ones. This is due to the larger area covered by the FOV of EUSO-TA at the long distances, which implies a higher number of showers in the FOV and, therefore, the aforementioned effect of photons arriving on the gaps is more likely to happen.

Table D.6
Parameters a and b of the lines $D = a \cdot E + b$ ($D \propto E$) and $D = a \cdot \sqrt{E} + b$ ($D \propto \sqrt{E}$) defining the detection limits from simulations of vertical showers, two elevation angles of EUSO-TA (10° and 25°), one version of the electronics board (SPACIROC1), and one background level (1 count/pixel/GTU). The a parameters have to be multiplied by the value indicated in the header of the table.

Background	Elevation	Parameters of the limit's equation	
(c./p./GTU)	(deg)	$a(\times 10^{-18}), b$ in $D \propto E$	$a(\times 10^{-8}), b$ in $D \propto \sqrt{E}$
1	10	3.06, −0.52	0.81, −4.50
1	25	6.26, −1.48	1.25, −7.19

Table D.7
Energy limit of EUSO-SPB1 estimated from simulations of vertical proton showers, two elevation angles of EUSO-TA (10° and 25°), one version of the electronics board (SPACIROC1), and one background level (1 count/pixel/GTU), for lines $D = a \cdot E + b$ ($D \propto E$) and $D = a \cdot \sqrt{E} + b$ ($D \propto \sqrt{E}$).

Background (c./p./GTU)	Elevation (deg)	$E^{\text{limit}}_{\text{EUSO-SPB1}}$ (eV)	
		$D \propto E$	$D \propto \sqrt{E}$
1	10	2.18×10^{18}	3.70×10^{18}
1	25	1.60×10^{18}	2.63×10^{18}
Average energy limit		$\mathbf{1.89 \times 10^{18}}$	$\mathbf{3.17 \times 10^{18}}$

In Table D.6 the parameters of the equations defining the detection limits are reported, considering both the forms $D = a \cdot E + b$ and $D = a \cdot \sqrt{E} + b$ and in Table D.7 the corresponding energy limits for EUSO-SPB1 are included. For the latter, the values are similar to those obtained with the simulation of showers with random directions, and this indicates the good performance of the methods used in the analysis.

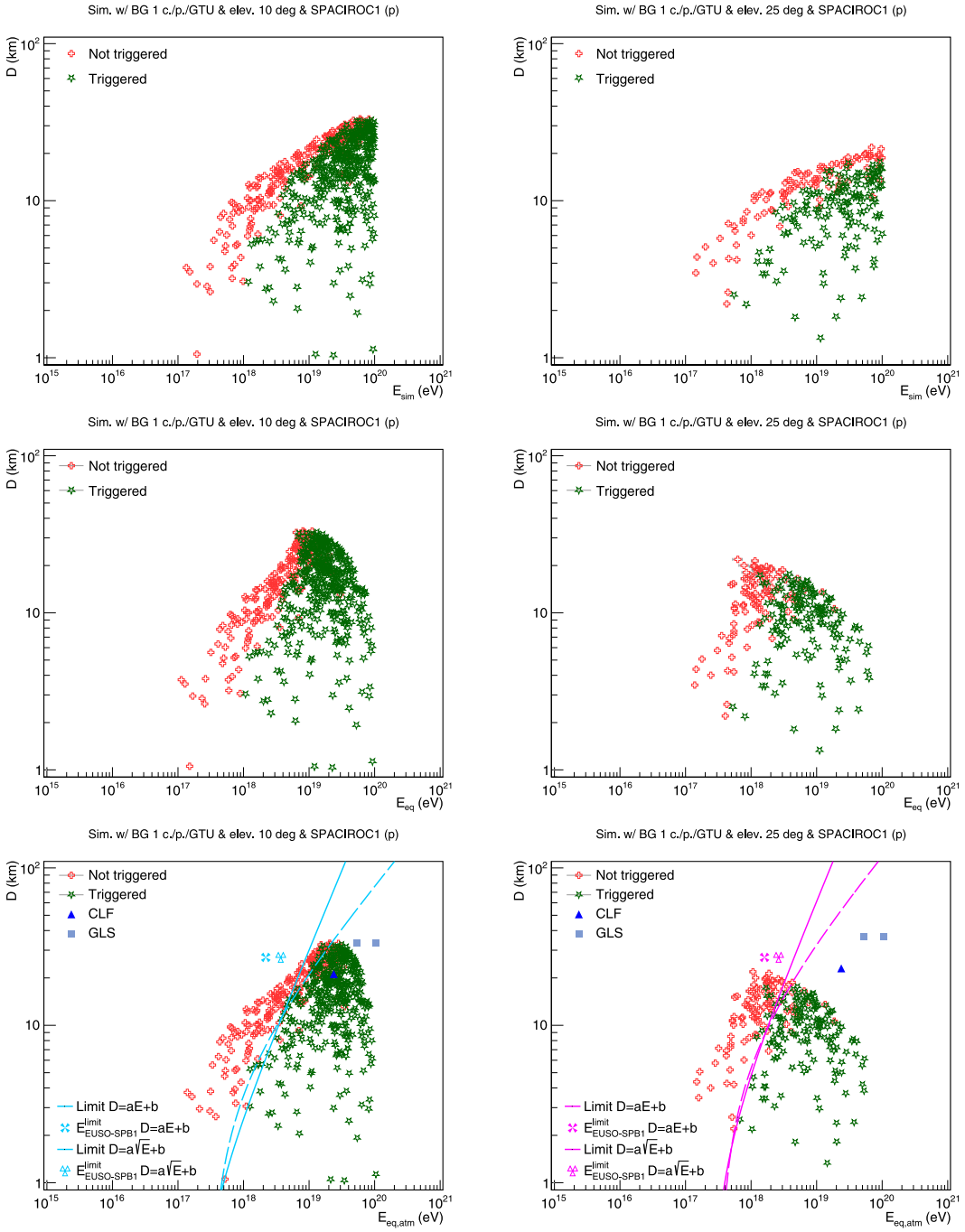

Fig. D.22. Simulated vertical proton showers in the FOV and the triggered ones represented with their distance to EUSO-TA measured inside the FOV and the simulated energy (top), the equivalent energy (middle), and the equivalent energy corrected for the atmospheric transmission (bottom), for 10° (left) and 25° (right) elevation angles. The simulated background is 1 count/pixel/GTU and the electronic board version is SPACIROC1. In the bottom plots, the distance and energy of laser events generated by the CLF and the GLS system are shown, too. In the same plots, the evaluated detection limit is drawn, as well as the evaluated limit of EUSO-SPB1.

Appendix E. Parameters of the detection limits from simulations

E.1. Distance versus energy

Table E.8 reports the a and b parameters of the lines representing the detection limits from proton simulations in the different background conditions (1 and 1.5 counts/pixel/GTU), elevation angles (10°, 15°, 20° and 25°), and with SPACIROC1 and SPACIROC3 electronics boards. Both the $D = a \cdot E + b$ and $D = a \cdot \sqrt{E} + b$ functions are used to evaluate the detection limit. The same information but for iron simulations is in Table E.9.

E.2. Counts versus Distance

See Tables E.10 and E.11.

E.3. Counts versus Energy

See Tables E.12 and E.13.

Table E.8
Parameters a and b of the lines $D = a \cdot E + b$ ($D \propto E$) and $D = a \cdot \sqrt{E} + b$ ($D \propto \sqrt{E}$) defining the detection limits from simulations proton showers and EUSO-TA with four elevation angles (10°, 15°, 20° and 25°), two versions of the electronics board (SPACIROC1 and SPACIROC3), and two background levels (1 and 1.5 counts/pixel/GTU). The a parameters have to be multiplied by the value indicated in the header of the table.

Proton			
Background	Elevation	Parameters of the limit's equation	
(c./p./GTU)	(deg)	SPACIROC1	
		$a(\times 10^{-18}), b$ in $D \propto E$	$a(\times 10^{-8}), b$ in $D \propto \sqrt{E}$
1	10	+4.97, −3.71	+1.40, −11.25
1	15	+2.04, +1.40	+0.56, −0.75
1	20	+8.32, −13.67	+4.98, −77.81
1	25	+5.90, −6.25	+1.64, −17.50
1.5	10	+2.29, −3.23	+0.78, −8.09
1.5	15	+2.85, −3.08	+0.88, −7.38
1.5	20	+3.49, −10.00	+1.34, −20.79
1.5	25	+3.18, −8.00	+0.93, −10.94
Background	Elevation	Parameters of the limit's equation	
(c./p./GTU)	(deg)	SPACIROC3	
		$a(\times 10^{-18}), b$ in $D \propto E$	$a(\times 10^{-8}), b$ in $D \propto \sqrt{E}$
1	10	+4.59, −2.38	+1.52, −13.99
1	15	+2.72, −0.29	+0.80, −4.35
1	20	+7.60, −11.02	+2.56, −32.33
1	25	+7.00, −4.59	+2.00, −18.35
1.5	10	+2.54, −3.50	+0.93, −8.81
1.5	15	+2.36, +0.50	+0.94, −8.25
1.5	20	+1.77, +2.48	+0.84, −7.50
1.5	25	+2.82, −0.27	+1.20, −12.79

Table E.9
Parameters a and b of the lines $D = a \cdot E + b$ ($D \propto E$) and $D = a \cdot \sqrt{E} + b$ ($D \propto \sqrt{E}$) defining the detection limits from simulations iron showers and EUSO-TA with four elevation angles (10°, 15°, 20° and 25°), two versions of the electronics board (SPACIROC1 and SPACIROC3), and two background levels (1 and 1.5 counts/pixel/GTU). The a parameters have to be multiplied by the value indicated in the header of the table.

Iron			
Background	Elevation	Parameters of the limit's equation	
(c./p./GTU)	(deg)	SPACIROC1	
		$a(\times 10^{-18}), b$ in $D \propto E$	$a(\times 10^{-8}), b$ in $D \propto \sqrt{E}$
1	10	+4.13, −3.00	+1.75, −19.08
1	15	+2.32, +2.38	+0.88, −5.14
1	20	+3.03, +1.75	+0.94, −5.25
1	25	+7.04, −7.91	+1.81, −18.81
1.5	10	+7.11, −47.85	+3.67, −93.85
1.5	15	+7.35, −49.32	+2.12, −42.25
1.5	20	+2.04, +0.25	+1.12, −13.75
1.5	25	+1.68, +2.50	+0.89, −9.00
Background	Elevation	Parameters of the limit's equation	
(c./p./GTU)	(deg)	SPACIROC3	
		$a(\times 10^{-18}), b$ in $D \propto E$	$a(\times 10^{-8}), b$ in $D \propto \sqrt{E}$
1	10	+6.48, −6.50	+1.34, −11.50
1	15	+2.32, +2.38	+0.88, −5.14
1	20	+5.74, −3.55	+1.50, −12.25
1	25	+5.78, −5.06	+5.46, −72.12
1.5	10	+3.54, −7.03	+1.02, −11.74
1.5	15	+1.81, +1.44	+0.85, −7.50
1.5	20	+2.94, −2.90	+1.22, −15.00
1.5	25	+6.54, −18.60	+2.76, −47.61

Table E.10
Parameters a and b of the lines separating triggered and non-triggered events depending on the number of counts and their distance $C = a \cdot D + b$ ($C \propto D$) or energy $C = a/D^2 + b$ ($C \propto 1/D^2$) defining the detection limits from simulations of proton showers and EUSO-TA with four elevation angles (10°, 15°, 20° and 25°), two versions of the electronics board (SPACIROC1 and SPACIROC3), and two background levels (1 and 1.5 counts/pixel/GTU).

Proton			
Background	Elevation	Parameters of the limit's equation	
(c./p./GTU)	(deg)	SPACIROC1	
		a, b in $C \propto D$	a, b in $C \propto 1/D^2$
1	10	−7.84, +504.74	+6373.00, +293.65
1	15	−6.32, +450.93	+1136.38, +222.32
1	20	−6.33, +407.80	+3288.52, +253.55
1	25	−8.82, +483.80	+6749.62, +284.23
1.5	10	−11.39, +724.60	+5139.73, +532.77
1.5	15	−10.79, +656.43	+9538.00, +357.43
1.5	20	−4.09, +482.06	+7387.21, +384.20
1.5	25	−6.60, +616.22	+5240.32, +497.53
Background	Elevation	Parameters of the limit's equation	
(c./p./GTU)	(deg)	SPACIROC3	
		a, b in $C \propto D$	a, b in $C \propto 1/D^2$
1	10	−6.71, +494.47	+8064.82, +298.27
1	15	−10.07, +528.44	+7227.70, +240.17
1	20	−9.56, +484.72	+4465.39, +253.88
1	25	−8.50, +429.28	+7538.18, +223.60
1.5	10	−11.33, +699.63	+7722.38, +476.47
1.5	15	−8.75, +593.33	+5984.98, +424.41
1.5	20	−11.78, +685.69	+6351.93, +439.01
1.5	25	−9.64, +624.31	+1000.00, +600.04

Table E.11
Parameters a and b of the lines separating triggered and non-triggered events depending on the number of counts C and their distance D $C = a \cdot D + b$ ($C \propto D$) or energy $C = a/D^2 + b$ ($C \propto 1/D^2$) defining the detection limits from simulations of iron showers and EUSO-TA with four elevation angles (10°, 15°, 20° and 25°), two versions of the electronics board (SPACIROC1 and SPACIROC3), and two background levels (1 and 1.5 counts/pixel/GTU).

Iron			
Background	Elevation	Parameters of the limit's equation	
(c./p./GTU)	(deg)	SPACIROC1	
		a, b in $C \propto D$	a, b in $C \propto 1/D^2$
1	10	−7.60, +458.62	+1778.50, +307.36
1	15	−5.55, +419.70	+6076.00, +290.71
1	20	−9.42, +484.69	+3742.92, +329.39
1	25	−9.20, +535.04	+4010.57, +345.24
1.5	10	−8.51, +668.47	+4240.00, +496.50
1.5	15	−8.37, +603.33	+9245.00, +436.58
1.5	20	−11.11, +749.31	+9802.00, +425.15
1.5	25	−8.58, +657.02	+7122.61, +477.48
Background	Elevation	Parameters of the limit's equation	
(c./p./GTU)	(deg)	SPACIROC3	
		a, b in $C \propto D$	a, b in $C \propto 1/D^2$
1	10	−7.57, +488.80	+9511.75, +276.49
1	15	−8.06, +486.63	+7975.36, +252.04
1	20	−5.11, +363.83	+7524.34, +203.54
1	25	−7.17, +443.11	+7099.26, +264.60
1.5	10	−11.6, +720.10	+7928.75, +386.94
1.5	15	−9.68, +611.53	+9470.34, +373.88
1.5	20	−9.03, +537.95	+3855.24, +385.16
1.5	25	−7.90, +607.46	+1958.26, +378.39

Table E.12
Parameters a and b of the lines separating triggered and non-triggered events depending on the number of counts and their distance $C = a \cdot D + b$ ($C \propto D$) or energy $C = a/D^2 + b$ ($C \propto 1/D^2$) defining the detection limits from simulated proton showers and EUSO-TA with four elevation angles (10°, 15°, 20° and 25°), two versions of the electronics board (SPACIROC1 and SPACIROC3), and two background levels (1 and 1.5 counts/pixel/GTU). The a parameters have to be multiplied by the value indicated in the header of the table.

Proton		
Background (c./p./GTU)	Elevation (deg)	Parameters of the limit's equation SPACIROC1 $a(\times 10^{-19}), b$ in $C \propto E$
1	10	−9.19, +353.92
1	15	−8.62, +233.28
1	20	−1.57, +356.58
1	25	−2.38, +344.92
1.5	10	−9.60, +558.77
1.5	15	−9.03, +473.27
1.5	20	−4.74, +434.49
1.5	25	−0.56, +528.76
Background (c./p./GTU)	Elevation (deg)	Parameters of the limit's equation SPACIROC3 $a(\times 10^{-19}), b$ in $C \propto E$
1	10	−9.10, +335.95
1	15	−9.77, +255.31
1	20	−9.39, +304.82
1	25	+0.55, +249.50
1.5	10	−9.08, +449.44
1.5	15	−7.20, +470.03
1.5	20	−8.76, +486.00
1.5	25	+4.20, +581.55

Table E.13
Parameters a and b of the lines separating triggered and non-triggered events depending on the number of counts and their distance $C = a \cdot D + b$ ($C \propto D$) or energy $C = a/x^2 + b$ ($C \propto 1/D^2$) defining the detection limits from simulated iron showers and EUSO-TA with four elevation angles (10°, 15°, 20° and 25°), two versions of the electronics board (SPACIROC1 and SPACIROC3), and two background levels (1 and 1.5 counts/pixel/GTU). The a parameters have to be multiplied by the value indicated in the header of the table.

Iron		
Background (c./p./GTU)	Elevation (deg)	Parameters of the limit's equation SPACIROC1 $a(\times 10^{-19}), b$ in $C \propto E$
1	10	−9.92, +321.40
1	15	−9.54, +326.80
1	20	−0.28, +332.76
1	25	−8.48, +362.77
1.5	10	−9.58, +539.56
1.5	15	−9.09, +475.85
1.5	20	−5.22, +455.04
1.5	25	+1.94, +542.17
Background (c./p./GTU)	Elevation (deg)	Parameters of the limit's equation SPACIROC3 $a(\times 10^{-19}), b$ in $C \propto E$
1	10	−7.31, +356.29
1	15	−9.22, +330.40
1	20	−3.34, +269.08
1	25	−2.33, +283.00
1.5	10	−8.80, +550.48
1.5	15	−8.95, +422.16
1.5	20	−9.56, +413.20
1.5	25	−7.43, +385.44

References

[1] E. Parizot, et al., The JEM-EUSO program for UHECR studies from space, EPJ Web Conf. 283 (2023) 06007.
[2] K. Greisen, End to the cosmic-ray spectrum? Phys. Rev. Lett. 16 (1966) 748.
[3] G.T. Zatsepin, V.A. Kuzmin, Upper limit of the spectrum of cosmic rays, Sov. Phys.—JETP 4 (1966).
[4] G. Abdellaoui, et al., (JEM-EUSO Coll.), EUSo-TA - first results from a ground-based EUSO telescope, Astropart. Phys. 102 (2018) 98–111.
[5] L.W. Piotrowski, (JEM-EUSO Coll.), Results and status of the EUSO-TA detector, in: PoS(ICRC2019), 2019, p. 388.
[6] M. Fukushima, et al., Telescope array project for extremely high energy cosmic rays, Progr. Theoret. Phys. Suppl. 151 (2003) 206–210.
[7] H. Tokuno, et al., New air fluorescence detectors employed in the Telescope Array experiment, Nucl. Instrum. Methods A 676 (2012) 54–65.
[8] Y. Takahashi, et al., Central laser facility analysis at the Telescope Array experiment, AIP Conf. Proc. 1367 (2011) 157–160.
[9] P. Hunt, et al., (JEM-EUSO Coll.), The JEM-EUSO global light system laser station prototype, in: PoS(ICRC2015), 2016, p. 626.
[10] A. Coleman, Ultra high energy cosmic rays the intersection of the cosmic and energy frontiers, Astropart. Phys. 149 (2023) 102819.
[11] Y. Hachisu, et al., (JEM-EUSO Coll.), Manufacturing of the TA-EUSO and the EUSO-Balloon lenses, in: Proceedings of ICRC2013, 2013, ID1040.
[12] H. Prieto-Alfonso, et al., (JEM-EUSO Coll.), Multi anode photomultiplier tube reliability assessment for the JEM-EUSO space mission, Reliab. Eng. Syst. Saf. 133 (2015) 137–145.
[13] J.H. Adams, et al., A review of the EUSO-balloon pathfinder for the JEM-EUSO program, Space Sci. Rev. 218 (2022) 3.
[14] L. Wiencke, et al., (JEM-EUSO Coll.), EUSo-SPB1 mission and science, in: PoS(ICRC2017), 2017, p. 1097.
[15] J. Eser, et al., Overview and first results of EUSO-SPB2, in: PoS(ICRC2023), 2023, p. 397.
[16] H. Miyamoto, et al., (JEM-EUSO Coll.), Performance of the SPACIROC front-end ASIC for JEM-EUSO, in: Proceedings of ICRC2013, 2013, ID1089.
[17] S. Blin-Bondil, et al., SPACIROC3: A Front-End Readout ASIC for JEM-EUSO cosmic ray observatory, in: PoS(TIPP2014), 2014, p. 172.
[18] M. Battisti, et al., (JEM-EUSO Coll.), Trigger developments for the fluorescence detector of EUSO-TA and EUSO-SPB2, in: PoS(ICRC2019), 2019, p. 426.
[19] A. Belov, et al., (JEM-EUSO Coll.), The integration and testing of the mini-EUSO multi-level trigger system, Adv. Space Res. 62 (2017) 2966–2976.
[20] R.U. Abbasi, et al., The energy spectrum of cosmic rays above 10 17.2 eV measured by the fluorescence detectors of the Telescope Array experiment in seven years, Astropart. Phys. 80 (2016) 131–140.
[21] L.W. Piotrowski, et al., On-line and off-line data analysis for the EUSO-TA experiment, Nucl. Instrum. Methods A 773 (2015) 164–171.
[22] T. Bergmann, et al., One-dimensional hybrid approach to extensive air shower simulation, Astropart. Phys. 26 (2007) 420–432.
[23] S. Ostapchenko, et al., Monte Carlo treatment of hadronic interactions in enhanced pomeron scheme: QGSJET-II model, Phys. Rev. D 83 (2011) 014018.
[24] D. Heck, et al., CORSIKA: A Monte Carlo code to simulate extensive air showers, in: Wissenschaftliche Berichte FZKA-6019, 1998.
[25] T. Tomida, et al., The atmospheric transparency measured with a LIDAR system at the Telescope Array experiment, Nucl. Instrum. Methods A 654 (2011) 653–660.
[26] S. Bacholle, et al., Mini-EUSO mission to study earth UV emissions on board the ISS, Astrophys. J. 520 (Suppl. 253) (2021) 36.
[27] T. Tomida, The atmospheric transparency of Telescope Array observation site by the CLF, in: PoS(ICRC2021)217.
[28] Auger Collaboration, The Pierre , techniques for measuring aerosol attenuation using the central laser facility at the Pierre Auger Observatory, JINST 8 (2013) P04009.
[29] T.C. Paul, et al., (JEM-EUSO Coll.), New simulation and reconstruction software for the EUSO pathfinders, with example applications, in: PoS(ICRC2017), 2017, p. 464.
[30] S. Abe, et al., EUSO-Offline: A comprehensive simulation and analysis framework, in: Prepared for Submission to JINST, 2023.
[31] J. Eser, The EUSO-SPB1 Project and Laser Test Beams for Space-Based Optical Cosmic Ray Detectors (Ph.D. thesis), 2018, https://hdl.h{and}le.net/11124/172510.
[32] R.U. Abbasi, et al., The energy spectrum of cosmic rays above $10^{17.2}$ eV measured by the fluorescence detectors of the telescope array experiment in seven years, Astropart. Phys. 80 (2016) 131–140.
[33] Pierre Auger Collaboration, The energy spectrum of cosmic rays beyond the turn-down around 10^{17} eV as measured with the surface detector of the Pierre Auger Observatory, Eur. Phys. J. C 81 (2021) 966.
[34] A. Aab, et al., Measurement of the cosmic-ray energy spectrum above 2.5×10^{18} eV using the Pierre Auger Observatory, Phys. Rev. D 102 (2020) 062005.
[35] N. Arsene, Mass composition of UHECRs from Xmax distributions recorded by the Pierre Auger and Telescope Array Observatories, Universe 7 (321) (2021) http://dx.doi.org/10.3390/universe7090321.